

Wave functions for high-symmetry, thin microstrip antennas, and two-dimensional quantum boxes

Joseph R. Rain ¹, PeiYu Cai ^{1,*}, Alexander Baekey ¹, Matthew A. Reinhard,^{1,2} Roman I. Vasquez,^{1,3}
 Andrew C. Silverman,¹ Christopher L. Cain ^{1,4} and Richard A. Klemm ^{1,5,†}

¹*Department of Physics, University of Central Florida, 4111 Libra Drive, Orlando, Florida 32816-2385, USA*

²*Department of Physics, University of Florida, 2001 Museum Road, P.O. Box 118440, Gainesville, Florida, 32611-8440, USA*

³*Department of Mathematics and Statistics, Auburn University, 221 Roosevelt Concourse, Auburn, Alabama 36849, USA*

⁴*Department of Natural Science, St. Petersburg College, Clearwater, Florida 37765, USA*

⁵*U.S. Research Laboratory, Wright-Patterson Air Force Base, Ohio 45433-7251, USA*



(Received 30 June 2021; revised 10 October 2021; accepted 30 November 2021; published 15 December 2021)

For a spinless quantum particle in a one-dimensional box or an electromagnetic wave in a one-dimensional cavity, the respective Dirichlet and Neumann boundary conditions both lead to nondegenerate wave functions. However, in two dimensions, the symmetry of the box or microstrip antenna is an important feature, the details of which have often been overlooked in the literature. In the high-symmetry cases of a disk, square, or equilateral triangle, the wave functions for both boundary conditions are grouped into two distinct classes, which are one- and two-dimensional representations of the respective point groups, $C_{\infty v}$, C_{4v} , and C_{3v} . Here we present visualizations of representative wave functions for both boundary conditions and both one- and two-dimensional representations of those point groups. For the nondegenerate or doubly degenerate one-dimensional representation wave functions, color contour plots are presented. The nominally doubly degenerate two-dimensional representation wave functions are presented as common nodal points and/or lines, the patterns of which are invariant under all operations of the respective point group. The wave functions with the Neumann boundary conditions have important consequences for the coherent terahertz emission from the intrinsic Josephson junctions in the high-temperature superconductor $\text{Bi}_2\text{Sr}_2\text{CaCu}_2\text{O}_{8+\delta}$: the enhancement of the output power from electromagnetic cavity resonances is strong only for nondegenerate wave functions.

DOI: [10.1103/PhysRevA.104.062205](https://doi.org/10.1103/PhysRevA.104.062205)

I. INTRODUCTION

The study of wave functions obtained from various geometries with Dirichlet and Neumann boundary conditions has been a useful educational resource and has numerous applications in the construction of various devices. A quantum particle in a one-dimensional (1D) infinite square well potential, or “box,” for which the boundary is a set of two points, is often the first problem studied by undergraduate students early in their first course on quantum mechanics [1]. Although three graduate texts contain two problems on the degeneracies of the lowest energies of a square two-dimensional (2D) box and of the 2D and three-dimensional (3D) simple harmonic oscillators (SHOs) [2–6], the solutions manuals for the first three texts and the 3D SHO in the fourth text did not mention that the doubly degenerate first excited state of the square box and of the 2D SHO and the sixfold degenerate first excited state of the 3D SHO were doubly or multiply degenerate, 2D representations of the appropriate point group, each component of which can be represented by an infinite number of spatial forms. Hence, there could be considerable confusion on this issue. Weinberger also included 2D box

and antenna problems with a variety of different or mixed boundary conditions [6].

Here we focus upon high-symmetry 2D shapes and will return to the 2D and 3D SHO in the summary and conclusions section. For a spinless quantum particle of mass M in a 2D infinite square well potential or box, the wave function $\psi(x, y, t)$ satisfies the Schrödinger equation,

$$-\frac{\hbar^2}{2M}\nabla^2\psi + V\psi = i\hbar\frac{\partial\psi}{\partial t}, \quad (1)$$

where $\hbar = \frac{h}{2\pi}$ and h is Planck’s constant, for which the potential $V(x, y) = 0$ inside the box and $V(x, y) = \infty$ outside it. Hence, $\psi(x, y, t) = 0$ outside the box and on its boundary, the simplest example of Dirichlet boundary conditions. Here we consider only closed 1D boundaries, and focus upon the 2D shapes with the highest point-group symmetries, $C_{\infty v}$, C_{4v} , and C_{3v} , corresponding to cylindrical, square, or equilateral triangular boxes [7–10].

For a thin (nearly 2D) microstrip antenna (MSA), the magnetic vector potential $A_z(x, y, t)$ normal to the antenna satisfies the electromagnetic (EM) wave equation

$$\nabla^2 A_z - \frac{1}{v^2} \frac{\partial^2 A_z}{\partial t^2} = 0, \quad (2)$$

where v is the wave velocity that depends upon the index of refraction in the antenna, and for transverse magnetic (TM) modes, its normal derivative vanishes on the boundary, the

*Present address: Imperial College London, Department of Physics, South Kensington Campus, London SW7 2AZ, United Kingdom.

†Corresponding author: richard.klemm@ucf.edu

simplest example of Neumann boundary conditions. Due to the oscillatory time dependence of a light wave, Eq. (2) is usually rewritten as $\nabla^2 A_z + (k')^2 A_z = 0$, where k' is the wave vector in the material of interest.

In particular, determining the symmetries and energy states of wave functions with Neumann boundary conditions is of great practical importance in the development of a high-power terahertz (THz) laser, which has many potential applications, such as for the detection of skin or colon cancer in humans and in secure communications. This is due to the ac Josephson effect, in which a dc voltage V is applied across a single junction, leading to an ac current I and the emission of photons at the frequency $f_J = 2eV/h$, where e is the charge of an electron [11]. Now there exist many layered superconductors [12], a number of which exhibit Josephson effects, but the most interesting one for the construction of a THz laser is the high transition temperature T_c superconductor $\text{Bi}_2\text{Sr}_2\text{CaCu}_2\text{O}_{8+\delta}$ (Bi2212). This material consists of a uniform stack of intrinsic Josephson junctions (IJJs) [13–16]. The output power P_1 of a single IJJ is about 1 pW, too small for most practical applications that require the actual power P to be at least 1 mW. But since each IJJ is 1.533 nm thick, a single crystal of Bi2212 of thickness 1 μm contains $N \approx 650$ IJJs, reducing f_J to

$$f_J = (2e/h)(V/N), \quad (3)$$

and when most of the N junctions emit coherently, ideally, $P_N = P_1 N^2 \approx 0.4 \mu\text{W}$. Moreover, in a thin mesa cut from a single crystal of Bi2212, the shape of the mesa acts as an electromagnetic cavity or MSA, which can enhance the output power an additional one to two orders of magnitude [16–20]. The emission frequency has to be larger than the Josephson plasma resonance frequency $f_p \approx 0.25$ THz [21]. In principle, the maximum emission frequency is the low temperature T value of the superconducting gap 2Δ , which is about 15 THz [22–24].

However, a major issue affecting the reliability and the upper limit of the emission frequency has been the Joule heating of the mesas [25–27], especially when they have Bi2212 substrates, since Bi2212 is a very poor thermal conductor. But this problem has been mostly removed by fabricating stand-alone mesas, in which the Bi2212 sample is doubly cleaved to a thickness of 1–2 μm from a single crystal, and the top and bottom surfaces are each coated with a thin layer of gold [18–20, 28–32]. These issues are discussed in Sec. VIII. When different parts of a small stand-alone Bi2212 single crystal were used both as the emitter and as the detector, emission up to 11 THz was observed [23]. An array of three stand-alone rectangular mesas was reported to emit coherently with the combined $P \approx 0.61$ mW [33], although an array of two rectangular mesas did not behave coherently [34], so the main concern for further development is the design of arrays to increase that number.

For low-symmetry rectangular boxes or MSAs, the wave functions are all nondegenerate, 1D representations (1DRs) of the point group C_{2v} . However, for the higher symmetry square [35–38], equilateral triangular [39–45], isosceles and right triangular [46, 47], regular pentagonal [48], cylindrical, disk [49, 50], annular [51], or singly slitted annular shapes [52], the situation can be considerably more complicated. Although some of the wave functions are nondegenerate 1DRs of the

respective point groups $C_{\infty v}$, C_{4v} , and C_{3v} under consideration here, a large fraction of the wave functions are nominally doubly degenerate 2D representations (2DRs) of those point groups, each component of which can be represented by an infinite number of real space forms [7–10]. In addition, for square and equilateral triangular boxes and MSAs, many additional wave functions are doubly degenerate 1DRs, each component of which can be represented only by a single spatial form. Previous works have calculated the dimensionality of the symmetry groups for the stationary states of the various wave functions, but there have not been thorough investigations of the features of the 2DRs of all three of these cases. Although for 2D boxes, such considerations are experimentally relevant only for deep quantum wells, for nearly 2D MSAs, the experimental consequences are very important, but have not been clearly described in the literature.

We note that circularly polarized coherent THz emission can be obtained by breaking the symmetry of square or disk MSAs [53–55], Bi2212 MSAs can be used both as emitters and as detectors [23, 56], and commercial cryocoolers can be used in cooling Bi2212 MSAs for many potential applications [57, 58]. Six review articles on Bi2212 IJJ-THz emitters have been published [59–64].

Here we present detailed studies of the wave functions for the three highest-symmetry 2D shapes: cylindrical boxes and disk MSAs, square boxes and MSAs, and equilateral triangular boxes and MSAs, in which either the wave function or its normal derivative vanishes on the boundary. Character tables of the respective point groups $C_{\infty v}$, C_{4v} , and C_{3v} are given in textbooks on group theory [7–10], but there are some minor differences in the wave function tables with Dirichlet and Neumann boundary conditions we present here, and some additions for the 2DR wave functions. In Sec. II we analyze the square box. In Sec. III we describe the thin square MSA. In Sec. IV we analyze the equilateral triangular box. In Sec. V we present the results for thin equilateral triangular MSA wave functions. In Sec. VI we show the cylindrical box wave functions. In Sec. VII we describe the disk MSA wave functions. In Sec. VIII we compare our results for square, equilateral triangular, and disk MSAs with published experimental results. Finally in Sec. IX we summarize our results for these high-symmetry boxes and MSAs, and discuss the possible relevance of the wave functions to degenerate perturbation theory in quantum mechanics and in Bose-Einstein condensates [65, 66].

II. THE SQUARE BOX

For a spinless quantum particle of mass M in a square box of side a , the normalized wave functions are solutions of the Schrödinger equation with $V(x, y) = 0$ for $0 < x, y < a$, $V(x, y) = \infty$ for $x, y \leq 0$ and $x, y \geq a$, which are

$$\Psi_{n,m}(x, y) = \frac{2}{a} \sin(n\pi x/a) \sin(m\pi y/a), \quad (4)$$

for integral $n, m \geq 1$, all of which satisfy the Dirichlet boundary conditions $\Psi_{n,m}(x, y) = 0$ for $x = 0, a$ and $y = 0, a$. The energy of that state is

$$E_{n,m} = \frac{\hbar^2(n^2 + m^2)\pi^2}{2Ma^2}. \quad (5)$$

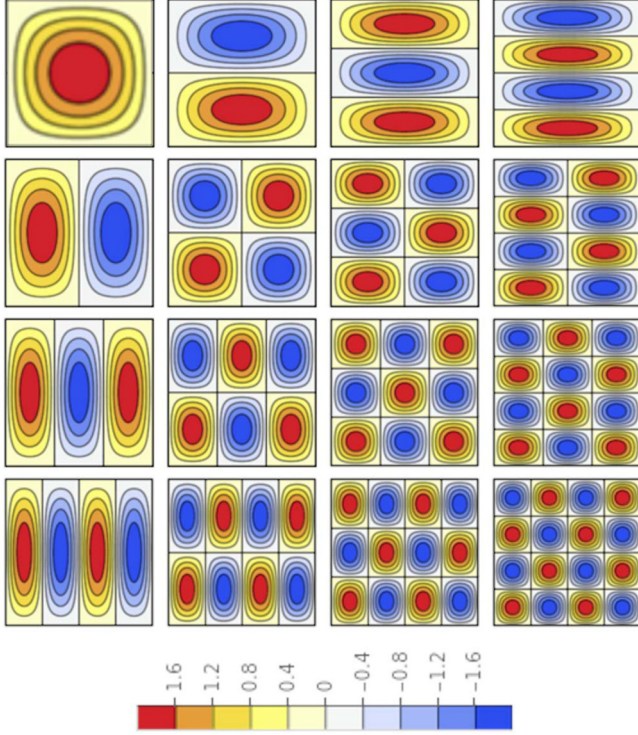


FIG. 1. Grid of color-coded plots of the normalized wave functions $\Psi_{n,m}(x, y) = \frac{2}{a} \sin(n\pi x/a) \sin(m\pi y/a)$ for a square box of side a with Dirichlet boundary conditions for $(n, m) = 1, 2, 3, 4$, each with its lower left corner at $(0,0)$. We set $a = 1$, and n and m are, respectively, the column and row numbers. The color code bar, which varies from -2.0 to $+2.0$, applies to each of these figures. The black boundaries and internal straight lines are nodes.

Figure 1 displays color-coded plots of the wave functions $\Psi_{n,m}(x, y)$ for $1 \leq n, m \leq 4$ of the square box.

According to the C_{4v} point group symmetry class [7–10], there are four mirror planes: the horizontal σ_h and vertical σ_v mirror planes that bisect the sides, and the two diagonal mirror planes, σ_{d1} and σ_{d2} , that bisect the corners. In addition, two rotations (R_4) by $2\pi/4$ and one (R_2) by π about the centroid are also allowed [7–10]. The wave functions fall into three basic classes. In the first class, $n = m$, $\Psi_{n,n}(x, y)$ is nondegenerate. But there are two subclasses of these nondegenerate wave functions. For n odd, the $\Psi_{n,n}(x, y)$ are invariant under all of these operations, whereas for n even, the $\Psi_{n,n}(x, y)$ are even about σ_{d1}, σ_{d2} and under R_2 , but are odd about σ_h, σ_v and under R_4 . According to Table I, the odd and even n $\Psi_{n,n}(x, y)$ are, respectively, elements of C_{4v} symmetry types A_1 and B_2 . The C_{4v} point group symmetry also applies to the orbital symmetry of the pairing function and of the distinct “pseudogap” (probably a charge density wave) in the cuprate superconductors, at least when the structural symmetry of the cuprate planes is not orthorhombic [67–69], a subject of continued interest for nearly three decades to date [22,24,67–71].

For $m = n + 2p + 1$, the pair of wave functions $\Psi_{n,n+2p+1}(x, y)$ and $\Psi_{n+2p+1,n}(x, y)$ are odd under R_2 , and have $I = 2$, the trace of the rank 2 identity matrix $\mathbf{1}$. The full

TABLE I. Square box representation types, symmetries, allowed 1DRs $\Psi_{n,n}(x, y)$ and $\Psi_{n,n+2p}^{(\pm)}(x, y)$ [Eq. (12)] for odd or even $n \geq 1$, 2DRs $\Psi_{n,n+2p+1}^{(\theta,\pm)}(x, y)$ [Eq. (6)] of the square box, and operations of the C_{4v} point group. $\sigma_h, \sigma_v, \sigma_{d1}$, and σ_{d2} are the mirror planes along the horizontal and vertical axes and the two diagonals, R_n represents rotations by $2\pi/n$ about the centroid, and I , usually written as E [10]), which could be confused with the energy, is the trace of the identity matrix for the appropriate group dimension. For the 2DR wave functions, the listed elements are the traces of the rank-2 matrices that describe the operations [10]. *Note that for the 2DR wave functions with only odd R_2 symmetry, their sets of common point nodes and square nodes all appear to have A_1 symmetry. †Under special conditions. See Figs. 3 and 4.

Type	Symmetry	$\Psi_{n,m}^{(\pm)}(x, y)$	n	I	R_2	$2R_4$	σ_h, σ_v	σ_{d1}, σ_{d2}
A_1	$x^2 + y^2$	$\Psi_{n,n}, \Psi_{n,n+2p}^{(+)}$	o	1	+1	+1	+1	+1
A_2	$xy(x^2 - y^2)$	$\Psi_{n,n+2p}^{(-)}$	e	1	+1	+1	-1	-1
B_1	$x^2 - y^2$	$\Psi_{n,n+2p}^{(-)}$	o	1	+1	-1	+1	-1
B_2	xy	$\Psi_{n,n}, \Psi_{n,n+2p}^{(+)}$	e	1	+1	-1	-1	+1
A_1^*	Point nodes	$\Psi_{n,n+2p+1}^{(\theta,\pm)}$	e, o	2	-2	0	0	0
A_1^*	Nodal squares†	$\Psi_{n,n+2p+1}^{(\theta,\pm)}$	e, o	2	-2	0	0	0

degeneracy can be represented by

$$\begin{aligned} \Psi_{n,n+2p+1}^{(\theta,+)}(x, y) &= \cos \theta \Psi_{n,n+2p+1}(x, y) \\ &\quad + e^{i\phi} \sin \theta \Psi_{n+2p+1,n}(x, y), \\ \Psi_{n,n+2p+1}^{(\theta,-)}(x, y) &= -\sin \theta \Psi_{n,n+2p+1}(x, y) \\ &\quad + e^{i\phi} \cos \theta \Psi_{n+2p+1,n}(x, y), \end{aligned} \quad (6)$$

which are the two orthonormal subsets of the degenerate $\Psi_{n,n+2p+1}(x, y)$ and $\Psi_{n+2p+1,n}(x, y)$ wave functions, as shown explicitly in the Appendix [36]. However, since $0 \leq \theta < 2\pi$, θ can be any real mixing angle, this double degeneracy has an infinite number of possible real space forms. For simplicity, we could assume that $\phi = 0$, so that the wave functions would all be real. This is entirely analogous to a spin $\frac{1}{2}$ system in the absence of a magnetic field, which is doubly degenerate from an infinite number of possible measurement directions [3]. In Fig. 2(a) this degeneracy is displayed for $\Psi_{1,2}^{(-\theta,+)}(x, y)$ for $\phi = 0$ at the three mixing angles $\theta = 60^\circ, 45^\circ$, and 30° , each of which is degenerate with its respective $\Psi_{1,2}^{(-\theta,-)}(x, y)$. In Fig. 2(b) the fact that such wave functions are odd under R_2 is evident for $\Psi_{2,1}(x, y)$ by adding $\Psi_{2,1}(x, y) + R_2 \Psi_{2,1}(x, y)$, which vanishes. The only points at which such wave functions are invariant under all of the operations of C_{4v} are their common nodal points. These wave functions are thus displayed for $1 \leq n, m \leq 4$ as the appropriate sets of nodal points in Fig. 3. We note that in each of these cases, the complete set of nodal points is invariant under each of the operations of C_{4v} (all four mirror planes and both rotations).

Writing these 2DR wave functions in the Nambu representation,

$$\Psi_{n,n+2p+1}^\theta(x, y) = \begin{pmatrix} \Psi_{n,n+2p+1}^{(\theta,+)}(x, y) \\ \Psi_{n,n+2p+1}^{(\theta,-)}(x, y) \end{pmatrix}, \quad (7)$$

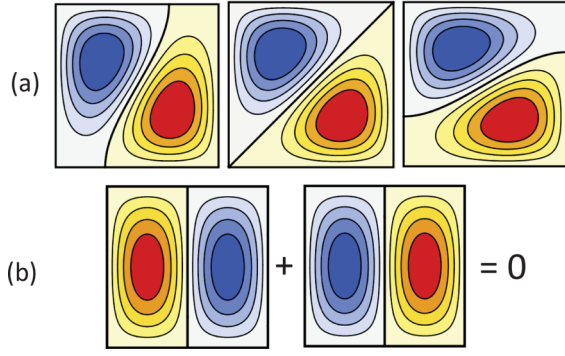


FIG. 2. (a) Color-coded plots of one component of the doubly degenerate 2DR square box wave function, each component of which can be presented in an infinite number of spatial forms, $\Psi_{1,2}^{(-\theta,+)}(x, y) = \cos \theta \Psi_{1,2}(x, y) - \sin \theta \Psi_{2,1}(x, y)$, for $\phi = 0$, $\theta = 60^\circ$ (left), 45° (center), and 30° (right). (b) Color-coded illustration of the oddness of $\Psi_{2,1}(x, y)$ under rotations about its centroid at $(\frac{a}{2}, \frac{a}{2})$ by π .

where the $\Psi_{n,n+2p+1}^{(\theta,\pm)}$ are given by Eq. (6) and the operations of C_{4v} upon them are rank-2 matrices. It is easy to show that $R_2 = -\mathbf{1}$, the trace of which is -2 . The other operations can be written in terms of the Pauli matrices σ_x , σ_y , and σ_z . In particular, the two R_4 matrices are

$\pm i\sigma_y$, $\sigma_h = \sigma_v = \sigma_z \cos(2\theta) - \sigma_x \sin(2\theta)$, and $\sigma_{d1} = -\sigma_{d2} = \sigma_z \sin(2\theta) + \sigma_x \cos(2\theta)$. Since the Pauli matrices are traceless, the traces of the two R_4 , σ_v , σ_h , σ_{d1} , and σ_{d2} all vanish for any value of θ .

More generally, one can write these 2DR wave functions for $n' = n + 2p + 1$ as

$$\Phi_{n,n'}(x, y) = \begin{pmatrix} \Phi_{n,n'}^{(1)}(x, y) \\ \Phi_{n,n'}^{(2)}(x, y) \end{pmatrix}, \quad (8)$$

where for $i = 1, 2$,

$$\Phi_{n,n'}^{(i)}(x, y) = \int_0^{2\pi} P(\theta) d\theta [A_i \Psi_{n,n'}^{(\theta,+)}(x, y) + B_i \Psi_{n,n'}^{(\theta,-)}(x, y)], \quad (9)$$

where $P(\theta) \neq C$, and where C is a constant. $P(\theta)$ is an arbitrary function whose only other restriction is that the generated wave functions are finite inside the box, and the A_i and B_i are chosen so that the $\Phi_{n,n'}^{(i)}(x, y)$ form an orthonormal set. For the perfectly random θ case, $P(\theta) = C$, the $\Phi_{n,n'}^{(i)}(x, y)$ for $i = 1, 2$ both vanish everywhere inside the box and cannot form an orthonormal pair. This perfectly random θ case thus implies complete wave function breakdown. Thus, $P(\theta) \neq C$ implies the θ values are correlated. We have assumed the square box to be perfect, without any imperfections such as cracks, distorted corners, or a spatially dependent potential $V(x, y)$ inside it. Hence, $P(\theta)$ describes a particular selection of the infinite number of degenerate spatial forms of the particular 2DR wave function.

As shown in more detail in the Appendix, orthonormalization with $P(\theta) \neq C$ leads for both $i = 1, 2$ to

$$|A_i|^2 + |B_i|^2 = [I_e^2 + I_o^2]^{-1}, \quad A_1 A_2^* + B_1 B_2^* = 0, \quad (10)$$

where

$$I_e = \int_0^{2\pi} P(\theta) \cos \theta d\theta, \quad I_o = \int_0^{2\pi} P(\theta) \sin \theta d\theta. \quad (11)$$

For $m = n + 2p$, there are again two classes. For n odd, $\Psi_{n,n+2p}(x, y)$ is even under reflections about σ_h , σ_v and under R_2 , but shows no symmetry under R_4 and about σ_{d1} , σ_{d2} . For n even, $\Psi_{n,n+2p}(x, y)$ is odd under reflections about σ_h , σ_v and under R_2 , but shows no symmetry under R_4 and about σ_{d1} , σ_{d2} . However, we note that for both n odd or even, $R_4 \Psi_{n,n+2p}(x, y) = \Psi_{n+2p,n}(x, y)$. This implies that there are two orthonormal members of each subgroup,

$$\Psi_{n,n+2p}^\pm(x, y) = \frac{1}{\sqrt{2}} [\Psi_{n,n+2p}(x, y) \pm \Psi_{n+2p,n}(x, y)], \quad (12)$$

which are doubly degenerate 1DRs of C_{4v} , each component of which has a single real space form. These wave functions for $n = 1, 2$ and $p = 1$ are also displayed in Fig. 3. $\Psi_{1,3}^+(x, y)$, which is shown in the top (first) row and third column of Fig. 3, is even under all of the operations of C_{4v} , and is therefore a 1DR of symmetry type A_1 . $\Psi_{1,3}^-(x, y)$, which is shown in the third row and first column of Fig. 3, is even under σ_h and σ_v , odd under σ_{d1} , σ_{d2} , and both R_4 operations (rotations by $\pm 2\pi/4$), and even under R_2 , is therefore a 1DR of C_{4v} symmetry type B_1 . Similarly, $\Psi_{2,4}^+(x, y)$, shown in the second row and fourth column of Fig. 3, is a 1DR of C_{4v} symmetry type B_2 , and $\Psi_{2,4}^-(x, y)$, shown in the fourth row and second column of Fig. 3, is a 1DR of C_{4v} symmetry type A_2 .

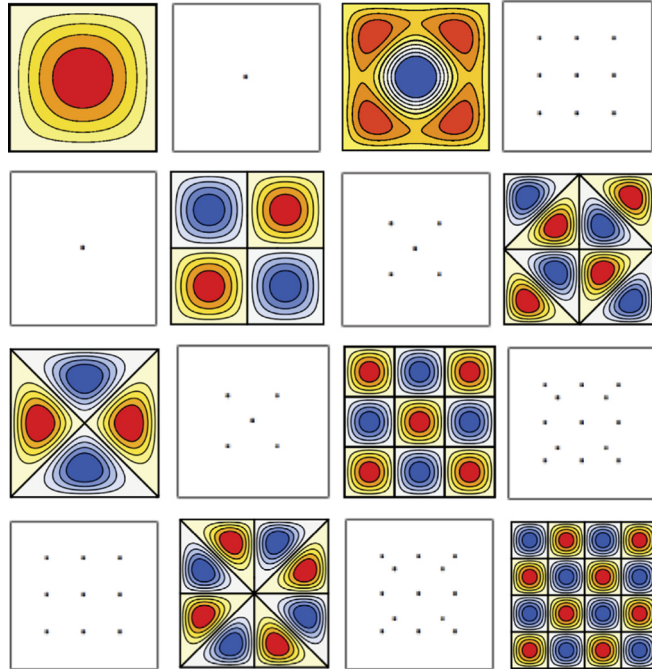


FIG. 3. Grid of color-coded plots of the 1DR square box wave functions $\Psi_{n,m}(x, y)$ with $1 \leq n, m \leq 4$. The nondegenerate $\Psi_{n,n}(x, y)$ are along the table diagonal, the doubly degenerate $\Psi_{n,n+2p}^+(x, y)$ and $\Psi_{n,n+2p}^-(x, y)$ are displayed in the regions above and below the diagonal, respectively, and the nominally doubly degenerate 2DR $\Phi_{n,n+2p+1}(x, y)$ given by Eqs. (8)–(11) are represented by their common nodal points. Each such set of common nodal points is a 1D representation of C_{4v} with symmetry type A_1 that is even under each of its symmetry operations: σ_h , σ_v , σ_{d1} , σ_{d2} , R_4 , and R_2 . The constant contours of the 1DR wave functions nearest to the boundary are parallel to it, due to the Dirichlet boundary conditions.

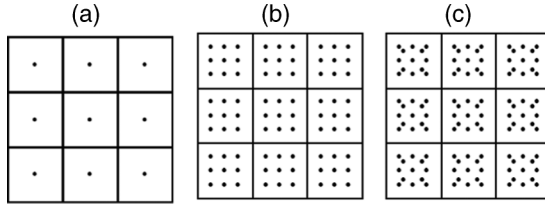


FIG. 4. Presentations of selected 2DRs with dots and squares. (a) $\Psi_{3,6}(x, y)$, $\Psi_{6,3}(x, y)$. (b) $\Psi_{3,12}(x, y)$, $\Psi_{12,3}(x, y)$. (c) $\Psi_{9,12}(x, y)$, $\Psi_{12,9}(x, y)$.

More generally, $\Psi_{n,n+2p}^+(x, y)$ for n odd is invariant under all C_{4v} operations, as seen in Fig. 3 for $\Psi_{1,3}^+(x, y)$. Hence, such wave functions have C_{4v} symmetry type A_1 and are listed as such in Table I. For n even, $\Psi_{n,n+2p}^+(x, y)$ is even under reflections about σ_{d1} , σ_{d2} and under R_2 , but is odd under reflections about σ_h , σ_v and under the two R_4 , so has symmetry type B_2 . For n odd, $\Psi_{n,n+2p}^-(x, y)$ is even under reflections about σ_h , σ_v and R_2 , but odd under reflections about σ_{d1} , σ_{d2} and under R_4 , so it has symmetry type B_1 . Finally, for n even, $\Psi_{n,n+2p}^-(x, y)$ is odd under reflections about all four mirror planes and under R_4 , but is even under R_2 , so it has symmetry type A_2 . These classifications are all listed in Table I.

In addition to the common nodal point structure of each of the doubly degenerate 2DR wave functions, each component of which has an infinite number of real space forms, some higher index 2DR wave functions have mutual nodal squares, a few of which are shown in Fig. 4. For such common nodal squares to appear in the common nodal set of 2DRs, the lower quantum number $n \geq 3$ must be odd. The lowest energy case is therefore the (3,6) case pictured in Fig. 4(a). In Fig. 4(b) the (3,12) case is shown. In addition, a more complicated nodal pattern is obtained for the (9,12) case pictured in Fig. 4(c). In this case, both numbers factor into three times an odd or an even number, and this factorization allows for the square common nodal structure, each of which encloses a finite set of common nodal dots. Obviously as the lower odd number increases, the common nodal patterns become increasingly complicated. But it is noteworthy that in every set of common nodal dots and/or squares that we found, that set is invariant under all operations of C_{4v} , and hence has the A_1 symmetry type. We have not tried to prove the generality of these observations.

III. THE SQUARE MICROSTRIP ANTENNA

For a thin square microstrip antenna of the same geometry as for the square box, with its origin at the lower left corner, but satisfying the EM wave equation for $A_z(x, y, t)$, the normalized transverse magnetic wave functions at a fixed time with the appropriate Neumann boundary conditions,

$$\frac{\partial \Psi_{n,m}(x, y)}{\partial x} \Big|_{x=0,a} = \frac{\partial \Psi_{n,m}(x, y)}{\partial y} \Big|_{y=0,a} = 0, \quad (13)$$

have the form

$$\Psi_{n,m}(x, y) = \begin{cases} \frac{2}{a} \cos(n\pi x/a) \cos(m\pi y/a), & m, n \geq 1 \\ \frac{\sqrt{2}}{a} \cos(n\pi x/a), & m = 0, n \geq 1. \\ \frac{\sqrt{2}}{a} \cos(m\pi y/a), & n = 0, m \geq 1 \end{cases} \quad (14)$$

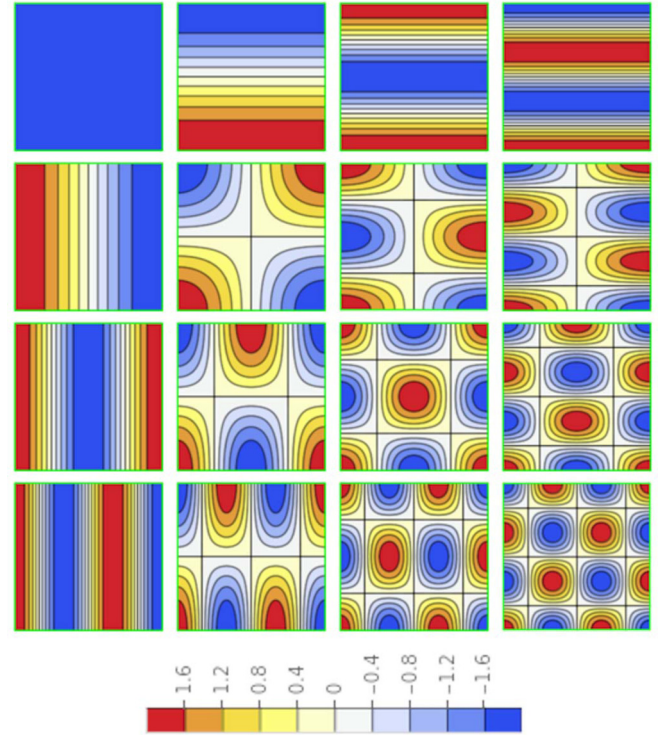


FIG. 5. Color-coded plots of the square MSA $\Psi_{n,m}(x, y)$ given by Eq. (14) for $0 \leq n, m \leq 3$, which are the nominal representations of the lowest-frequency wave functions of a square microstrip antenna with Neumann boundary conditions that are indicated by the green boundaries. n and m are, respectively, the column and row numbers. $\Psi_{0,0} = 1/a$ shown in blue corresponds to frequency $f_{0,0} = 0$, so it is excluded. The color code bar, which varies from -2.0 to $+2.0$, otherwise applies to each of these figures.

The enhanced emission frequencies $f_{n,m}$ from the square thin MSA are

$$f_{n,m} = c_0 \frac{\sqrt{n^2 + m^2}}{2an_r}, \quad (15)$$

where c_0 is the vacuum speed of light and n_r is the index of refraction, which for Bi2212 IJJ-THz emitter devices that are on the order of $1 \mu\text{m}$ thick, is about 4.2. The case $n = m = 0$ must be excluded, since light must have a finite frequency. In this case, the color-coded lowest-frequency square MSA wave functions are shown in Fig. 5.

As for the square box wave functions, the $n = m$ MSA wave functions are all nondegenerate 1DRs of the C_{4v} point group, and the $m = n + 2p + 1$ MSA wave functions are doubly degenerate 2DRs of C_{4v} , having the $\Phi_{n,n+2p+1}^{(i)}(x, y)$ component forms of Eqs. (8)–(11), which can be presented by an infinite number of spatial forms, except that the wave function components are given by Eq. (14) instead of Eq. (4). This second point is illustrated in Fig. 6. In addition, since the MSA wave functions satisfy $\Psi_{n,n+2p}(x, y) = R_4 \Psi_{n+2p,n}(x, y)$, exactly as for the square box, these wave functions are doubly degenerate 1DRs, each component of which has a single spatial form, and satisfy Eq. (12), although again with the wave function components given by Eq. (14). The symmetry table of the square MSA wave functions is therefore shown in

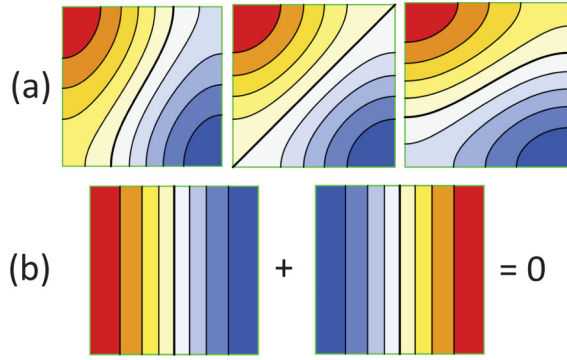


FIG. 6. (a) Color-coded plots of the square MSA 2DR $\Psi_{0,1}^{(-\theta,+)}(x, y)$ for $\theta = 30^\circ, 45^\circ$, and 60° from left to right. (b) Plot of $\Psi_{0,1}(x, y) + R_2\Psi_{0,1}(x, y)$, which equals 0.

Table II. The only differences between Table II and Table I for the square box is that the oddness or evenness of the quantum number n is precisely the opposite, and there are no nodal squares for the square MSA 2DR wave functions. The matrices that describe the symmetry operations upon the 2DR MSA wave functions are identical to those presented for the square quantum box wave functions following Eq. (7).

We then redisplay those and additional MSA wave functions in the array shown in Fig. 7. As for the square box, the diagonal $n = m$ square MSA wave functions are all non-degenerate 1DRs of C_{4v} , and are displayed in color-coded contour plots. The doubly degenerate 2DR $m = n + 2p + 1$ cases, each component of which has an infinite number of spatial forms, are again displayed as a set of mutually common nodal points, but in this MSA case, as discussed in more detail in the following, there are no mutual nodal lines for any index number. Furthermore, the $m = n + 2p$ cases are doubly degenerate 1DRs, with the $\Psi_{n,n+2p}^\pm(x, y)$ given by Eq. (12) with the appropriate MSA wave functions, and with the $\Psi_{n,n+2p}^+$ displayed above the diagonal, and the $\Psi_{n,n+2p}^-$ displayed below the array diagonal, exactly as in Fig. 3 for the box. Note

TABLE II. Square MSA representation types, symmetries, allowed 1DRs $\Psi_{n,n}(x, y)$ and $\Psi_{n,n+2p}^{(\pm)}(x, y) = [\Psi_{n,n+2p}(x, y) \pm \Psi_{n+2p,n}(x, y)]/\sqrt{2}$ for odd or even $n \geq 1$, 2DRs $\Psi_{n,n+2p+1}^{(\theta,\pm)}(x, y)$, which have the forms of Eqs. (6)–(11), except that their components satisfy Eqs. (13) and (14), and the same operations of the C_{4v} point group as in Table I. For the 2DR wave functions, the listed values are the traces of the rank-2 matrices that describe the operations [10]. *Note that the 2DR wave functions have only odd R_2 symmetry, but each of their sets of common fixed point nodes appears to have A_1 symmetry. See Ref. [36].

Type	Symmetry	$\psi_{n,n}^{(\pm)}(x, y)$	n	I	R_2	$2R_4$	σ_h, σ_v	σ_{d1}, σ_{d2}
A_1	$x^2 + y^2$	$\Psi_{n,n}, \Psi_{n,n+2p}^{(+)}$	e	1	+1	+1	+1	+1
A_2	$xy(x^2 - y^2)$	$\Psi_{n,n+2p}^{(-)}$	o	1	+1	+1	-1	-1
B_1	$x^2 - y^2$	$\Psi_{n,n+2p}^{(-)}$	e	1	+1	-1	+1	-1
B_2	xy	$\Psi_{n,n}, \Psi_{n,n+2p}^{(+)}$	o	1	+1	-1	-1	+1
A_1	Point nodes*	$\Psi_{n,n+2p+1}^{(\theta,\pm)}$	e, o	2	-2	0	0	0

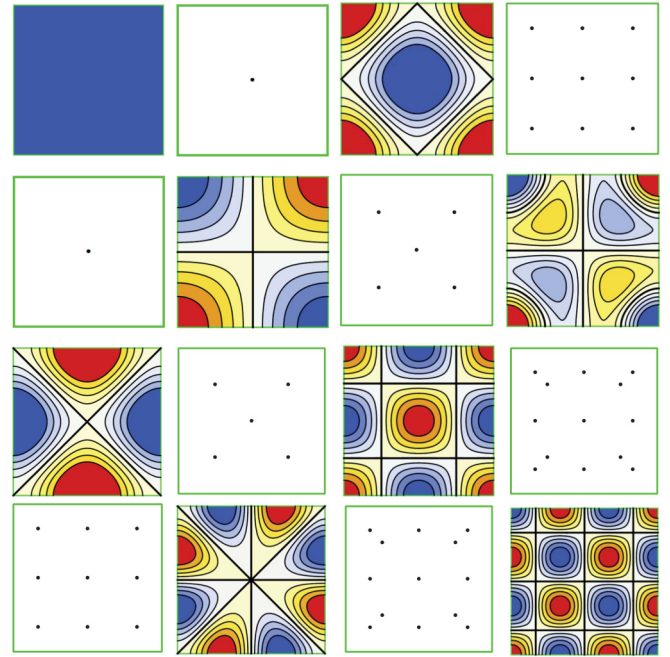


FIG. 7. Shown are plots of the array of square MSA wave functions $\Psi_{n,m}(x, y)$ with Neumann boundary conditions for $0 \leq n, m \leq 3$. 1DR wave functions of nondegenerate $\Psi_{n,n}$ (for $n \geq 1$) and doubly degenerate 1DR wave functions $\Psi_{n,n+2p}^\pm$, each component can be shown only in a single spatial form, are shown in color-coded plots along the array diagonal and in the appropriate positions above (below) that diagonal. Plots of the nominally doubly degenerate 2DRs $\Psi_{n,n+2p+1}^{(\theta,\pm)}$, each component of which can be presented in an infinite number of ways, are represented as arrays of black mutual nodal points, all appearing to be invariant under all C_{4v} operations. The constant contours nearest to a boundary intersect it normally due to the Neumann boundary conditions.

that in Fig. 7, $\Psi_{0,2}^+(x, y)$ and $\Psi_{0,2}^-(x, y)$ have respective C_{4v} symmetry types A_1 and B_1 , and $\Psi_{1,3}^+(x, y)$ and $\Psi_{1,4}^-(x, y)$ have respective C_{4v} symmetry types B_2 and A_2 . The symmetry types of $\Psi_{n,n}(x, y)$ and $\Psi_{n,n+2p}^{(\pm)}(x, y)$ for n even or odd are given in Table II, and are opposite to those of the analogous square box functions listed in Table I.

For the square box 2DR wave functions with $n, m > 0$ without any line nodes, the number of point nodes is $N(n, m) = (n - 1)^2 + (m - 1)^2$. Similarly, for $n, m \geq 0$, the number of square MSA point nodes in a 2DR is $N(n, m) = n^2 + m^2$. However, as argued in the following, no nodal lines or squares appear in the square MSA 2DRs. But as for the square box, the set of common nodal points for each 2DR is invariant under all operations of C_{4v} , and hence obeys the A_1 symmetry table.

A nodal line could occur along the x direction if $\cos(n\pi x/a) = 0$ for $0 < x < a$ and along the y direction if $\cos(m\pi y/a) = 0$ for $0 < y < a$. These require $x/a = (2p + 1)/(2n)$ and $y/a = (2q + 1)/(2m)$ for integer p and q . For them to occur together and the pattern to be invariant under

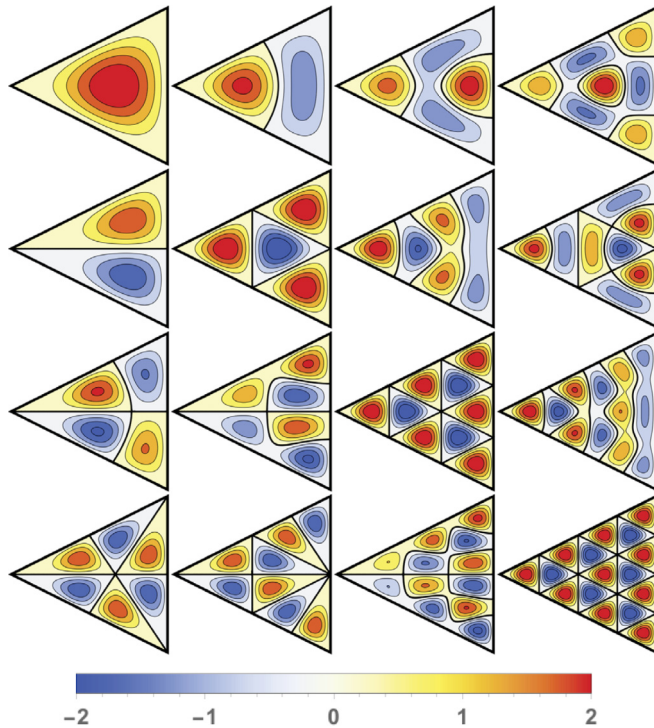


FIG. 8. Array of color-coded plots of the lowest-energy, normalized equilateral triangular box wave functions with $n, m = 1, 2, 3, 4$ from Eqs. (17), (18), and (21). The array diagonal consists of 1DR wave functions that are invariant under all C_{3v} operations. The figures above and below the diagonal are, respectively, even and odd about the horizontal axis. The color code bar that varies from -2.0 to $+2.0$ applies to each of these figures.

functions can be generated. The equilateral triangular box wave functions even and odd about that axis can be written as

$$\Psi_{\ell,m,n}^e(x,y) = A_{m,n}^e \left\{ \sin \left[\left(\frac{2\pi x}{\sqrt{3}a} + \frac{2\pi}{3} \right) \ell \right] \cos \left[\frac{2\pi(m-n)y}{3a} \right] + \sin \left[\left(\frac{2\pi x}{\sqrt{3}a} + \frac{2\pi}{3} \right) m \right] \cos \left[\frac{2\pi(n-\ell)y}{3a} \right] + \sin \left[\left(\frac{2\pi x}{\sqrt{3}a} + \frac{2\pi}{3} \right) n \right] \cos \left[\frac{2\pi(\ell-m)y}{3a} \right] \right\} \quad (17)$$

and

$$\Psi_{\ell,m,n}^o(x,y) = A_{m,n}^o \left\{ \sin \left[\left(\frac{2\pi x}{\sqrt{3}a} + \frac{2\pi}{3} \right) \ell \right] \sin \left[\frac{2\pi(m-n)y}{3a} \right] + \sin \left[\left(\frac{2\pi x}{\sqrt{3}a} + \frac{2\pi}{3} \right) m \right] \sin \left[\frac{2\pi(n-\ell)y}{3a} \right] + \sin \left[\left(\frac{2\pi x}{\sqrt{3}a} + \frac{2\pi}{3} \right) n \right] \sin \left[\frac{2\pi(\ell-m)y}{3a} \right] \right\}. \quad (18)$$

Since each of the three terms for the even and odd wave functions must satisfy the Schrödinger equation $-\frac{\hbar^2}{2M}\nabla^2\Psi = E\Psi = \frac{\hbar^2 k^2}{2M}\Psi = 0$, this is equivalent to the EM wave equation, $\nabla^2\Psi + k^2\Psi = 0$. Since for each wave function form, each term must separately satisfy that wave equation, we find

$$(n-m)(\ell+n+m) = 0, \quad (19)$$

as for the equilateral MSA [45]. As for the antenna, the $n = m$ cases can be shown to not produce any additional wave functions, so we assume $\ell = -n - m$. However, in this case,

the operations of C_{4v} , including R_4 , which interchanges x and y , we then require

$$\frac{2p+1}{2n} = \frac{2q+1}{2m}. \quad (16)$$

As noted from Table II, if $n = m$, $\Psi_{n,n}(x,y)$ is a nondegenerate 1DR, and if n and m are either both odd or both even, then $\Psi_{n,n+2p}^\pm(x,y)$ is a doubly degenerate combination of two 1DRs. But if either n or m is odd and the other is even, then the $\Phi_{n,n+2p+1}(x,y)$ wave functions are doubly degenerate 2DRs, each component of which can be presented in an infinite number of spatial forms, and the corresponding box wave functions can have additional nodal boxes. However, for the square MSA, by rewriting Eq. (16) as $(2p+1)m = (2q+1)n$, it is easy to see that this criterion for additional nodal boxes cannot be satisfied with either n or m odd and the other even.

IV. THE EQUILATERAL TRIANGULAR BOX

Previous studies have focused on the 1DR wave functions of equilateral triangular MSAs [45]. Here we calculate the quantum wave functions and normalization constants for the equilateral triangle of side a in an infinite potential well. The Schrödinger equation admits even and odd wave function solutions about any of the symmetry axes. Here we choose the horizontal axis as the axis of symmetry from which the wave

both the odd and even wave functions vanish on the entire equilateral triangular boundary.

The energies for a quantum particle of mass M in an equilateral triangular quantum box are then found to be

$$E_{n,m} = \frac{(4\pi\hbar)^2}{2M(3a)^2}(m^2 + n^2 + mn), \quad (20)$$

which is $\propto k^2$ for the equilateral triangular MSA. The corresponding normalization coefficients are obtained by integrating $|\Psi_{\ell,m,n}^{o,e}|^2$ with $\ell = -n - m$ over the area of the

equilateral triangle, and dividing by that area. We find

$$A_{m,n}^e = \begin{cases} \frac{4}{3^{3/4}a}, & m > n \neq 0, \quad n > m \neq 0 \\ \frac{2\sqrt{2}}{3^{3/4}a}, & m = n, \end{cases}$$

$$A_{m,n}^o = \frac{4}{3^{3/4}a}, \quad m > n \neq 0, \quad n > m \neq 0. \quad (21)$$

These equilateral triangular box normalization constants are remarkably similar to those obtained for the equilateral triangular MSA [45], as shown in Sec. IV. The normalized equilateral triangular box wave functions $\Psi_{n,m}^{(e,o)}(x, y)$ are pictured for $n, m = 1, 2, 3, 4$ in Fig. 8.

To illustrate examples of the equilateral triangular box wave functions that are even or odd about only one vertex, we show pictorially for 2DR equilateral triangular box wave functions that

$$|\Psi_{2,3}^{(e,o)}(x, y)\rangle + R_3 |\Psi_{2,3}^{(e,o)}(x, y)\rangle + R_3^2 |\Psi_{2,3}^{(e,o)}(x, y)\rangle = 0, \quad (22)$$

where we have used the Dirac ket notation.

These equations show that only two of the wave functions even or odd about only one vertex are linearly independent, demonstrating that these wave functions are 2DR wave functions. Thus, we could choose as the general basis $|\Psi_{n,m}^{(e,o)}(x, y)\rangle$ and $R_3 |\Psi_{n,m}^{(e,o)}(x, y)\rangle$, where $m \neq n + 3p$.

But since these wave functions are not orthonormal, we set

$$|\Psi_{n,m}^{(e,o,1)}(x, y)\rangle = A |\Psi_{n,m}^{(e,o)}(x, y)\rangle + BR_3 |\Psi_{n,m}^{(e,o)}(x, y)\rangle,$$

$$|\Psi_{n,m}^{(e,o,2)}(x, y)\rangle = C |\Psi_{n,m}^{(e,o)}(x, y)\rangle + DR_3 |\Psi_{n,m}^{(e,o)}(x, y)\rangle, \quad (23)$$

for constants A, B, C , and D , and force them to form an orthonormal set.

To do so, we first take the inner product of Eq. (22) with $\langle \Psi_{n,m}^{(e,o)}(x, y) | R_3^\dagger$, and it is easily seen that

$$\langle \Psi_{n,m}^{(e,o)}(x, y) | R_3^\dagger | \Psi_{n,m}^{(e,o)}(x, y) \rangle = -\frac{1}{2}. \quad (24)$$

Although complex coefficients are possible, especially for $|A| > \frac{2}{\sqrt{3}}$, under the assumption that all coefficients are real, it is then easy to show that the orthonormal set can be written as

$$|\Psi_{n,m \neq n+3p}^{(e,o,1,\theta,\pm)}(x, y)\rangle = \frac{2}{\sqrt{3}} \cos \theta |\Psi_{n,m}^{(e,o)}(x, y)\rangle$$

$$+ \left(\frac{1}{\sqrt{3}} \cos \theta \pm \sin \theta \right) R_3 |\Psi_{n,m}^{(e,o)}(x, y)\rangle,$$

$$|\Psi_{n,m \neq n+3p}^{(e,o,2,\theta,\pm)}(x, y)\rangle = -\frac{2}{\sqrt{3}} \sin \theta |\Psi_{n,m}^{(e,o)}(x, y)\rangle$$

$$- \left(\frac{1}{\sqrt{3}} \sin \theta \mp \cos \theta \right) R_3 |\Psi_{n,m}^{(e,o)}(x, y)\rangle, \quad (25)$$

where $0 \leq \theta < 2\pi$ is arbitrary. These wave functions can be represented with either the two upper signs or the two lower signs, but not both, so that they are doubly degenerate 2DR wave functions that can be pictured in an infinite number of spatial forms.

TABLE III. Representation types, symmetries, allowed 1DRs $\Psi_{n,n+3p}^{(e,o)}(x, y)$ and 2DRs $\Psi_{n,m \neq n+3p}^{(o,e,\theta)}(x, y)$ of the equilateral triangular box, and operations of the C_{3v} point group. For 1DR wave functions, there are three mirror planes σ_v that bisect each angle, two rotations R_3 by $\pm 2\pi/3$ about the centroid, and I is the trace of the identity matrix for the appropriate group dimension [10]. The 2DR wave functions have only one σ_v . *Common nodal structure. See Figs. 9–11.

Type	Symmetry	$\psi_{n,m}^{(e,o)}(x, y)$	I	$2R_3$	$3\sigma_v$
A_1	$x^2 + y^2$	$\Psi_{n,n+3p}^e(x, y)$	1	+1	+1
A_2	$y(3x^2 - y^2)$	$\Psi_{n,n+3p}^o(x, y)$	1	+1	-1
A_1^*	Nodal points	$\Psi_{n,m \neq n+3p}^{(o,e,\theta)}$ n, m not both even	2	-1	0
A_1^*	Nodal points	$\Psi_{n,m \neq n+3p}^{(o,e,\theta)}$, n, m both even and triangles	2	-1	0

When acting on the Nambu form of these 2DR wave functions analogous to that in Eq. (7) for the square box,

$$|\Psi_{n,m \neq n+3p}^{(e,o,\theta,\pm)}(x, y)\rangle = \begin{pmatrix} |\Psi_{n,m \neq n+3p}^{(e,o,1,\theta,\pm)}(x, y)\rangle \\ |\Psi_{n,m \neq n+3p}^{(e,o,2,\theta,\pm)}(x, y)\rangle \end{pmatrix}, \quad (26)$$

the matrices R_3 and R_3^\dagger are

$$R_3 = -\frac{1}{2} \mathbf{1} \pm i \frac{\sqrt{3}}{2} \sigma_y, \quad (27)$$

and its Hermitian conjugate, both traces of which are -1 , as indicated in Table III.

With regard to the mirror symmetry operations of a 2DR wave function about a single vertex, the even wave functions satisfy $\sigma_v^{(e)} |\Psi_{n,m}^{(e,\theta)}\rangle = |\Psi_{n,m}^{(e,\theta)}\rangle$, $\sigma_v^{(e)} R_3 |\Psi_{n,m}^{(e,\theta)}\rangle = R_3^2 |\Psi_{n,m}^{(e,\theta)}\rangle$ and $\sigma_v^{(e)} R_3^2 |\Psi_{n,m}^{(e,\theta)}\rangle = R_3 |\Psi_{n,m}^{(e,\theta)}\rangle$, as evidenced from Fig. 9(a). Combining these equations with Eq. (22), it is then straightforward to show that the mirror plane matrix $\sigma_v^{(e)}$ when acting on the Nambu form of Eq. (26) can be written for the even functions as

$$\sigma_v^{(e)} = \frac{\sigma_z}{2} [\cos(2\theta) \mp \sqrt{3} \sin(2\theta)]$$

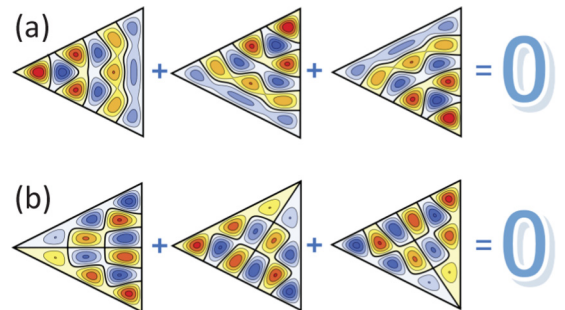


FIG. 9. Even (a) and odd (b) examples of 2DR equilateral triangular box wave functions pictured in Fig. 8, each satisfying the picture equation $|\Psi\rangle + R_3 |\Psi\rangle + R_3^2 |\Psi\rangle = 0$. In these examples, $(n, m) = (2, 3)$.

$$-\frac{\sigma_x}{2}[\sin(2\theta) \pm \sqrt{3}\cos(2\theta)], \quad (28)$$

which is traceless, as indicated in Table III. On the other hand, the 2DR wave functions odd about one vertex satisfy $\sigma_v^{(o)}|\Psi_{n,m}^{(o,\theta)}\rangle = -|\Psi_{n,m}^{(o,\theta)}\rangle$, $\sigma_v^{(o)}R_3|\Psi_{n,m}^{(o,\theta)}\rangle = -R_3^2|\Psi_{n,m}^{(o,\theta)}\rangle$ and $\sigma_v^{(o)}R_3^2|\Psi_{n,m}^{(o,\theta)}\rangle = -R_3|\Psi_{n,m}^{(o,\theta)}\rangle$, as sketched in Fig. 9(b). Again, combining these equations with Eq. (22), when acting upon the odd Nambu form of Eq. (25), $\sigma_v^{(o)} = -\sigma_v^{(e)}$, which is given by Eq. (28), so that both traces of $\sigma_v^{(e)}$ and $\sigma_v^{(o)}$ vanish, as indicated in Table III.

But in generalizing to an arbitrary function $P(\theta) \neq C$, which is further restricted only to require the wave functions to be finite in magnitude inside the equilateral triangular box, as was done in Eqs. (8)–(11) for the 2DR square box wave functions and the square MSA, we then can write

$$|\Phi_{n,m}^{(e,o,\pm)}(x,y)\rangle = \begin{pmatrix} |\Phi_{n,m}^{(e,o,1,\pm)}(x,y)\rangle \\ |\Phi_{n,m}^{(e,o,2,\pm)}(x,y)\rangle \end{pmatrix}, \quad (29)$$

for $m \neq n + 3p$, where

$$|\Phi_{n,m}^{(e,o,i,\pm)}(x,y)\rangle = \int_0^{2\pi} d\theta P(\theta) [A_i |\Psi_{n,m}^{(e,o,1,\theta,\pm)}(x,y)\rangle + B_i |\Psi_{n,m}^{(e,o,2,\theta,\pm)}(x,y)\rangle], \quad (30)$$

which is a linear combination of the two types of \pm wave functions. The wave functions form an orthonormal set, provided that the A_i and B_i satisfy Eqs. (10) and (11), as for the square box and MSA.

As for the square box, we then redraw the 2DR equilateral triangular box wave functions in terms of their common sets of nodes. This results in the array pictured in Fig. 10. We note that $\Psi_{1,4}^e(x,y)$ and $\Psi_{4,1}^o(x,y)$ pictured in the top right and bottom left array positions are doubly degenerate 1DRs, as are all four of the $\Psi_{n,n}^e(x,y)$ along the array diagonal. In addition, $\Psi_{2,4}^e(x,y)$ and $\Psi_{2,4}^o(x,y)$ are both 2DRs that contain an identical set of nodal points plus a single equilateral triangular nodal figure in their center. Additional examples of nodal points and equilateral triangles are pictured in Fig. 11. We note that both with and without the equilateral triangular nodal lines inside the box, the loci of points and lines in each 2DR is invariant under all of the operations of C_{3v} . Therefore, we classify those nodal loci as having symmetry A_1 in Table III. We note that the common internal equilateral triangular nodal figures arise only for $(n, m \neq n + 3p)$ both even.

V. THE EQUILATERAL TRIANGULAR MICROSTRIP ANTENNA

Although the wave functions for the thin equilateral triangular MSA were given previously [45], those authors plotted only the 1DR wave functions and calculated the angular distributions of the output power from those resonant cavity modes and from the uniform Josephson current source at those mode frequencies. Here we are primarily interested in contrasting the pictorial representation of the 1DR and 2DR wave functions. We have

$$\Psi_{\ell,m,n}^e(x,y) = A_{m,n}^e \left\{ \cos \left[\left(\frac{2\pi x}{\sqrt{3}a} + \frac{2\pi}{3} \right) \ell \right] \cos \left[\frac{2\pi(m-n)y}{3a} \right] + \cos \left[\left(\frac{2\pi x}{\sqrt{3}a} + \frac{2\pi}{3} \right) m \right] \cos \left[\frac{2\pi(n-\ell)y}{3a} \right] + \cos \left[\left(\frac{2\pi x}{\sqrt{3}a} + \frac{2\pi}{3} \right) n \right] \cos \left[\frac{2\pi(\ell-m)y}{3a} \right] \right\} \quad (31)$$

and

$$\Psi_{\ell,m,n}^o(x,y) = A_{m,n}^o \left\{ \cos \left[\left(\frac{2\pi x}{\sqrt{3}a} + \frac{2\pi}{3} \right) \ell \right] \sin \left[\frac{2\pi(m-n)y}{3a} \right] + \cos \left[\left(\frac{2\pi x}{\sqrt{3}a} + \frac{2\pi}{3} \right) m \right] \sin \left[\frac{2\pi(n-\ell)y}{3a} \right] + \cos \left[\left(\frac{2\pi x}{\sqrt{3}a} + \frac{2\pi}{3} \right) n \right] \sin \left[\frac{2\pi(\ell-m)y}{3a} \right] \right\}. \quad (32)$$

Each of the three terms for the even and odd wave functions must satisfy the EM wave equation $\nabla^2\Psi + (k')^2\Psi = 0$, as for the square MSA. These forms can be shown to also obey the Neumann boundary conditions. As for the equilateral triangular box, we again have

$$(n-m)(\ell+n+m) = 0, \quad (33)$$

and the same arguments for $n = m$ in Sec. IV lead to the conclusion $\ell = -n - m$ [45].

The emission frequencies $f_{n,m}$ from an equilateral triangular MSA with index of refraction n_r are then found to be

$$f_{n,m} = \frac{2c_0}{3an_r} \sqrt{m^2 + n^2 + mn}. \quad (34)$$

The corresponding normalization coefficients are obtained by integrating $|\Psi_{\ell,m,n}^{o,e}|^2$ over the area of the equilateral triangle, and dividing by that area. As was found previously [45],

$$A_{m,n}^e = \begin{cases} \frac{4}{3^{3/4}a}, & m, n \geq 1, \quad m \neq n \\ \frac{2\sqrt{2}}{3^{3/4}a}, & m > n = 0, n > m = 0, \quad \text{or} \quad m = n, \end{cases} \quad (35)$$

$$A_{m,n}^o = \begin{cases} \frac{4}{3^{3/4}a}, & m, n \geq 1, \quad m \neq n, \\ \frac{2\sqrt{2}}{3^{3/4}a}, & m > n = 0, \quad \text{or} \quad n > m = 0, \end{cases}$$

and all of the odd equilateral triangular MSA wave functions with $m = n$ vanish. As shown in the previous section, these normalization constants are remarkably similar to those obtained for the equilateral triangular box. The normalized

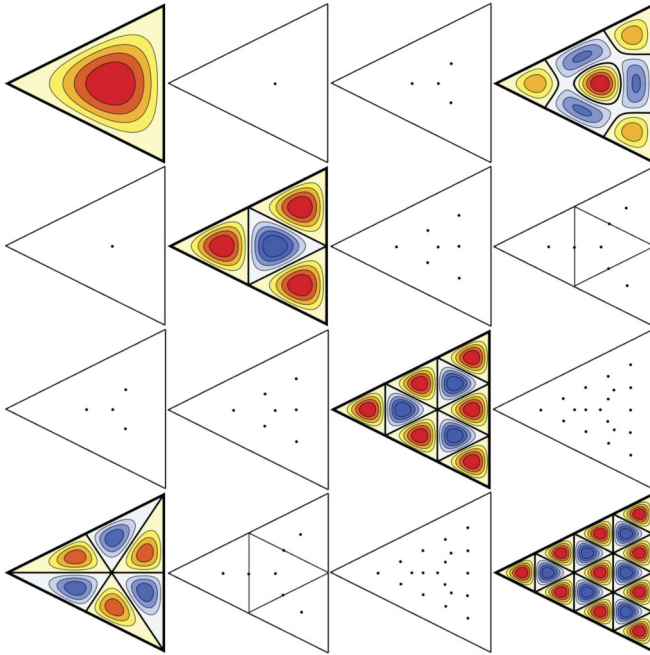


FIG. 10. Plots of the same equilateral triangular box wave functions pictured in Fig. 8, but displaying the 2DR wave functions in terms of their loci of common nodes. The upper right $\Psi_{1,4}^e(x, y)$ and lower left $\Psi_{4,1}^o(x, y)$ are doubly degenerate 1DRs.

equilateral triangular MSA wave functions $\Psi_{n,m}^{(e,o)}(x, y)$ are pictured for $n, m = 0, 1, 2, 3$ in Fig. 12.

As for the 2DR wave functions for the equilateral triangular box that satisfy Eq. (22), the 2DR wave functions for the thin equilateral triangular MSA exhibit the same symmetries. For example, in Fig. 13 we show pictorially that

$$|\Psi_{3,4}^{(e,o)}(x, y)\rangle + R_3|\Psi_{3,4}^{(e,o)}(x, y)\rangle + R_3^2|\Psi_{3,4}^{(e,o)}(x, y)\rangle = 0, \quad (36)$$

the only difference being the wave functions are not the box wave functions with Dirichlet boundary conditions given by Eqs. (17)–(21), but are instead given by Eqs. (31)–(35) for the MSA, which satisfy the Neumann boundary conditions with the normal derivative vanishing on each of the triangle’s sides. Therefore, the 2DR wave functions can be constructed exactly by analogy with Eqs. (22)–(25), also leading to the analogous Nambu representation and to the rank 2 matrices representing the identical symmetry operations R_3 and $\sigma_v^{(e,o)}$ given by Eqs. (27) and (28). These thin equilateral MSA wave functions are also doubly degenerate 2DRs of the C_{3v} point

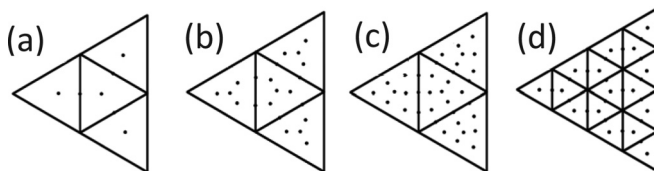


FIG. 11. Shown are some examples of higher index equilateral triangular box 2DR wave functions represented by both common points and equilateral triangles. (a) $\Psi_{2,4}^{(e,o)}$; (b) $\Psi_{2,6}^{(e,o)}$; (c) $\Psi_{4,6}^{(e,o)}$; (d) $\Psi_{4,8}^{(e,o)}$.

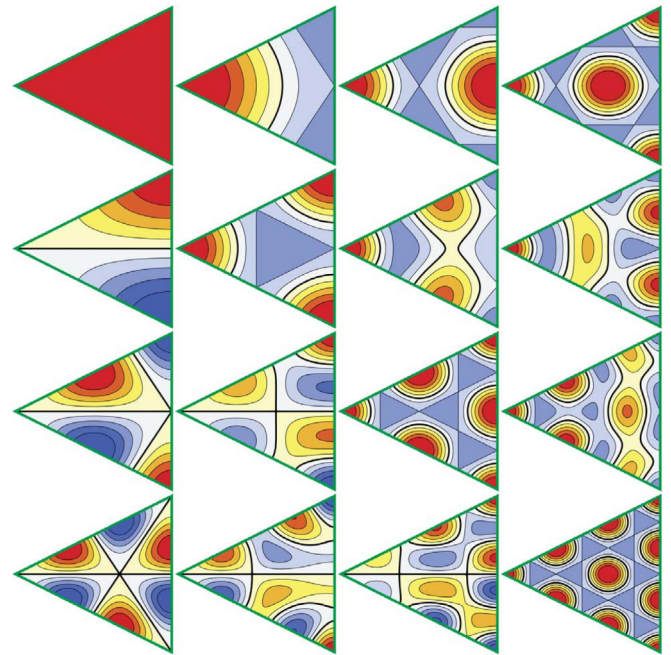


FIG. 12. Array of color-coded plots of the lowest-frequency equilateral triangular microstrip antenna wave functions, generated from Eqs. (31), (32), and (35), with $n, m = 0, 1, 2, 3$. The upper left solid red figure has $f_{0,0} = 0$, so it can be excluded. The diagonal of the array represents $\Psi_{n,n}^e(x, y)$, which for $n > 0$ are 1DRs. The $n \neq m$ even and odd wave functions lie respectively above and below the array diagonal. The green boundaries indicate the Neumann conditions. The color code bar displayed in Fig. 8 applies to each of these figures except the excluded (0,0) case.

group, as they also contain the arbitrary analogous mixing angle θ and can be pictured in an infinite number of spatial forms. The representation types, symmetries, and allowed 1DR and 2DR wave functions for the equilateral triangular MSA are presented in Table IV. Pictorial representations of equilateral triangular MSA wave functions corresponding to those presented in Fig. 10 for the equilateral triangular box are pictured in Fig. 14. Thus, of the equilateral triangular MSA wave functions pictured, those in color are 1DRs, and those along the array diagonal and in the upper right figure have A_1 symmetry, and the figure in the lower left has A_2 symmetry.

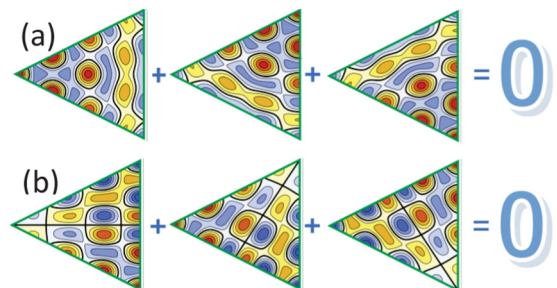


FIG. 13. (a) Even $|\Psi_{3,4}^e(x, y)\rangle$ and odd (b) $|\Psi_{3,4}^o(x, y)\rangle$ examples of 2DR equilateral triangular MSA wave functions not pictured in Fig. 12 that each satisfies the picture equation $|\Psi\rangle + R_3|\Psi\rangle + R_3^2|\Psi\rangle = 0$.

TABLE IV. Representation types, symmetries, allowed 1DRs $\Psi_{n,n+3p}^{e,o}(x, y)$ and 2DRs $\Psi_{n,m\neq n+3p}^{(o,e)}(x, y)$ of the thin equilateral triangular MSA, and operations of the C_{3v} point group. For the 1DR wave functions, there are three mirror planes σ_v that bisect each angle, two rotations R_3 by $\pm 2\pi/3$ about the centroid, and I is the trace of the identity matrix for the appropriate group dimension. For the 2DR wave functions, there are the same rotations, but only one σ_v [10]. *Common nodal points. See Fig. 13.

Type	Symmetry	$ \Psi_{n,m}^{(e,o)}(x, y)\rangle$	I	$2R_3$	$3\sigma_v$
A_1	$x^2 + y^2$	$ \Psi_{n,n+3p}^e(x, y)\rangle$	1	+1	+1
A_2	$y(3x^2 - y^2)$	$ \Psi_{n,n+3p}^o(x, y)\rangle$	1	+1	-1
A_1^*	Fixed point nodes	$ \Psi_{n,m\neq n+3p}^{(o,e,\theta)}\rangle$	2	-1	0

The rest of the figures are 2DRs, and the pattern of nodal points has A_1 symmetry that is invariant under all operations of point group C_{3v} . The matrices representing the $2R_3$ and single σ_v operations of the C_{3v} point group acting upon the 2DR wave functions are identical to those described for the equilateral triangular box, except that the spatial parts of the wave functions are given by Eqs. (31) and (32).

As for the 2DR wave functions for the square box and MSA, the 2DR wave functions for the equilateral triangular MSA have the same forms as for the equilateral triangular box, obeying Eqs. (24)–(30), except that the bare wave functions are given by Eqs. (31)–(35). Thus, the 2DR wave functions for the equilateral triangular MSA also have two (\pm) alternative ways of writing the components, each of which can be presented by an infinite number of spatial forms, to the corresponding doubly degenerate wave functions. The

TABLE V. $\chi_{m,p} = k_{m,p}a$ for the cylindrical box of radius a . Missing entries correspond to higher energy states than pictured in Fig. 15.

m	$\chi_{m,1}$	$\chi_{m,2}$	$\chi_{m,3}$	$\chi_{m,4}$
0	2.4048	5.52007	8.65372	11.79153
1	3.8317	7.01558	10.1734	13.32369
2	5.13562	8.41724	11.61984	14.795981
3	6.38016	9.76102	13.01520	16.22346
4	7.58834	10.64709	14.3725	
5	8.77148	12.3386	15.70017	
6	9.936109	13.58929	17.0038	
7	11.08637	14.821268		
8	12.22509	16.03777		

only difference between Tables III and IV for the equilateral triangular box and the thin equilateral triangular MSA is that some (with m and n both even) of the 2DR box wave functions contain both common nodal points and internal equilateral triangles (as well as on the boundary), but the 2DR MSA wave functions contain only common nodal points. In both cases, the loci of the sets of nodal points and/or triangles are invariant under all operations of point group C_{3v} .

VI. THE CYLINDRICAL BOX

For a quantum particle in a cylindrical box of radius a , the Schrödinger equation is written in polar coordinates. $V(\rho) = 0$ for $0 \leq \rho < a$, and $V(\rho) = \infty$ for $\rho \geq a$. Using separation of variables and assuming $\Psi(\rho, \phi + 2\pi) = \Psi(\rho, \phi)$, one obtains the Bessel equation with solutions of the first kind. Since $\Psi(\rho, \phi)$ must be finite inside the cylindrical box, we have only the integer Bessel functions of the first kind, $J_m(k_m\rho)$ multiplied by $\sin(m\phi)$ or $\cos(m\phi)$. Therefore a general state can be written

$$\Psi_m(\rho, \phi) = [B_m \cos(m\phi) + C_m \sin(m\phi)]J_m(k_m\rho). \quad (37)$$

For the cylindrical box of radius a , we require $\Psi_m(a, \phi) = 0$, or

$$J_m(k_m a) = 0. \quad (38)$$

Since there are many possible zeros of $J_m(x)$, we index them with $k_{m,p}$ values. Thus, we set

$$J_m(k_{m,p}a) = 0, \quad (39)$$

$$\Psi_{m,p}(\rho, \phi) = [B_{m,p} \cos(m\phi) + C_{m,p} \sin(m\phi)]J_m(k_{m,p}\rho). \quad (40)$$

It is immediately obvious that the cases $m = 0$ and $m \geq 1$ are qualitatively different. For $m = 0$, the wave functions $\Psi_{0,p}(\rho)$ are 1DRs independent of ϕ . For $m \geq 1$, the wave functions are all 2DRs. Since $\cos(m\phi)$ and $\sin(m\phi)$ are orthogonal when integrated over ϕ from 0 to 2π , we could write either $B_{m,p} = A_{m,p} \cos(m\theta)$ and $C_{m,p} = A_{m,p} \sin(m\theta)$ or $B_{m,p} = -A_{m,p} \sin(m\theta)$ and $C_{m,p} = A_{m,p} \cos(m\theta)$. Thus, the wave functions that are 2DRs of the $C_{\infty v}$ point group can be

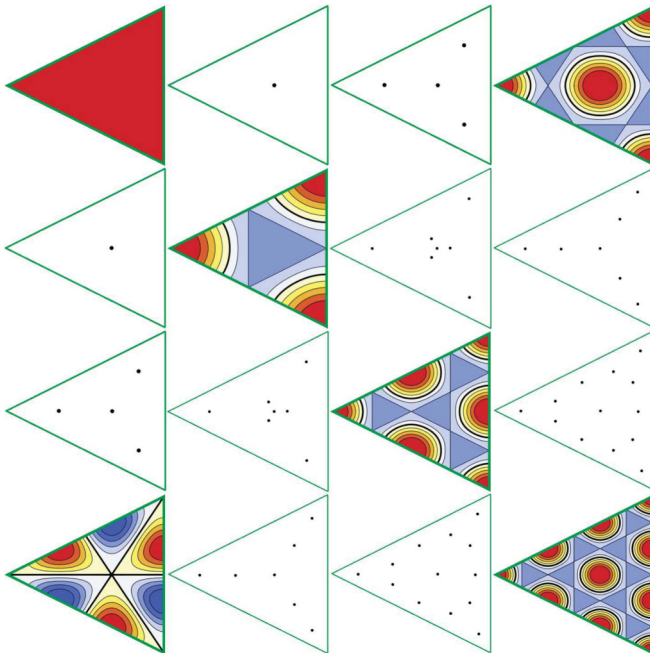


FIG. 14. Plots of the same equilateral triangular MSA wave functions pictured in Fig. 12, but displaying the 2DR wave functions in terms of their loci of common nodes. The upper right $\Psi_{1,4}^{(e)}(x, y)$ and lower left $\Psi_{4,1}^{(o)}(x, y)$ wave functions are doubly degenerate 1DRs.

written in Nambu form as

$$\begin{aligned} \Psi_{m,p}^\theta(\phi, \rho) &= \begin{pmatrix} \Psi_{m,p}^{(\theta,1)}(\phi, \rho) \\ \Psi_{m,p}^{(\theta,2)}(\phi, \rho) \end{pmatrix} \\ &= A_{m,p} J_m(k_{m,p} \rho) \begin{pmatrix} \cos[m(\phi - \theta)] \\ \sin[m(\phi - \theta)] \end{pmatrix}, \end{aligned} \quad (41)$$

where θ satisfying $0 \leq \theta < 2\pi$ is a 2DR wave function mixing angle as for the 2DR wave functions of the square and equilateral triangular boxes, and the $A_{m,p}$ are found by normalization of both $|\Psi_{m,p}^{(\theta,1)}(\rho, \phi)|^2$ and $|\Psi_{m,p}^{(\theta,2)}(\rho, \phi)|^2$ over the cross-sectional area of the cylinder,

$$A_{m,p} = \begin{cases} \frac{1}{a\sqrt{\pi} \int_0^1 x dx J_m^2(\chi_{m,p} x)}, & m \geq 1 \\ \frac{1}{a\sqrt{2\pi} \int_0^1 x dx J_0^2(\chi_{0,p} x)}, & m = 0 \end{cases} \quad (42)$$

$$\chi_{m,p} = k_{m,p} a.$$

The energy of the (m, p) mode for a spinless quantum particle of mass M in the cylindrical box is given by

$$E_{m,p} = \frac{\hbar^2 \chi_{m,p}^2}{2Ma^2}. \quad (43)$$

A list of $\chi_{m,p}$ values for $0 \leq m \leq 8$ and $1 \leq p \leq 4$ is given in Table V.

As for the 2DR wave functions for the square and equilateral triangular boxes, we can also generalize Eq. (41) to include an arbitrary distribution of θ values, rewriting it for $i = 1, 2$ and $m \geq 1$ as

$$\Psi_{m,p}^{(i)}(\phi, \rho) = \int_0^{2\pi} P(\theta) d\theta [A_i \Psi_{m,p}^{(\theta,1)}(\phi, \rho) + B_i \Psi_{m,p}^{(\theta,2)}(\phi, \rho)], \quad (44)$$

where again $P(\theta) \neq C$ is restricted to yield finite 2DR wave functions inside the disk box. In this case, the orthonormalization of the 2DR wave functions includes both Eq. (42) and

$$|A_i|^2 + |B_i|^2 = [I_{m,e}^2 + I_{m,o}^2]^{-1}, \quad A_1 A_2^* + B_1 B_2^* = 0 \quad (45)$$

where

$$\begin{aligned} I_{m,e} &= \int_0^{2\pi} d\theta P(\theta) \cos(m\theta), \\ I_{m,o} &= \int_0^{2\pi} d\theta P(\theta) \sin(m\theta). \end{aligned} \quad (46)$$

In Fig. 15 we have presented an array of the 16 lowest-energy wave functions for a quantum particle in a cylindrical box. However, from Eq. (41), it is evident that the angle θ is arbitrary. Since $0 \leq \theta < 2\pi$, it can take on an infinite number of values, and hence cylindrical box eigenstates with $m \neq 0$ are doubly degenerate 2DRs of the $C_{\infty v}$ point group, each component of which can be presented in an infinite number of spatial forms. In Fig. 16 this arbitrary θ value is illustrated by comparing $\Psi_{2,2}(\rho, \phi)$ with $\theta = 0$ and with its orientation with $\theta = 53^\circ$. Hence, those cylindrical box wave functions with straight line nodes passing through their centroids are indeed 2DRs of the $C_{\infty v}$ point group. Other than the circular line nodes at fixed ρ , the straight line nodes that can be rotated

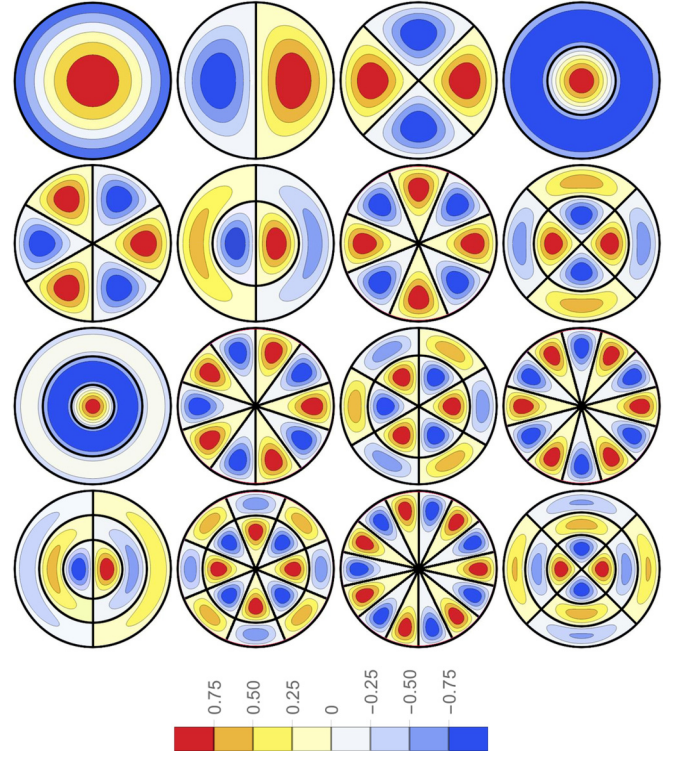


FIG. 15. Color-coded plots of the 16 lowest-energy cylindrical box wave functions, all oriented with $\theta = 0$ and ranked in order from the top left to the bottom right array positions, listed as (m, p) : Top row: (0,1), (1,1), (2,1), (0,2). Second row: (3,1), (1,2), (4,1), (2,2). Third row: (0,3), (5,1), (3,2), (6,1). Fourth row: (1,3), (4,2), (7,1), (2,3). Each figure has a qualitatively similar but numerically distinct color code bar that varies from -0.96 to $+0.96$ is for the (2,2) mode. Colors for the (0,1) mode represent only different wave function magnitudes.

have only the single node at their common origin, the centroid. This is illustrated in Fig. 17.

In order to construct Table VI, the symmetry table for the cylindrical box, we first note that for $m \geq 1$, Eq. (41) contains two components, $\Psi_{m,p}^{(\theta,1)}(\phi, \rho)$ and $\Psi_{m,p}^{(\theta,2)}(\phi, \rho)$, which form the orthonormal components of a 2DR wave function. When the two rotation matrices $R_{\pm m\varphi}$ for rotations by $\pm m\varphi$ about the z -axis normal to the centroid act on this Nambu form for the 2DR wave function, they are easily found to be $R_{\pm m\varphi} = \mathbf{1} \cos(m\varphi) \pm i\sigma_y \sin(m\varphi)$, the traces of which are $2 \cos(m\varphi)$. This rotation matrix changes θ to $\theta \pm \varphi$ in the

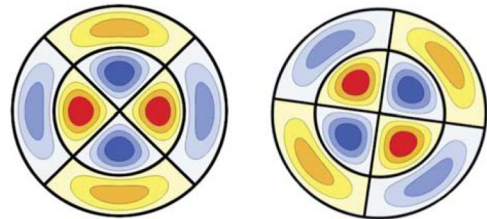


FIG. 16. Color-coded plots of $\Psi_{2,2}(\rho, \phi)$ with $\theta = 0^\circ$ (left), and $\theta = 53^\circ$ (right).

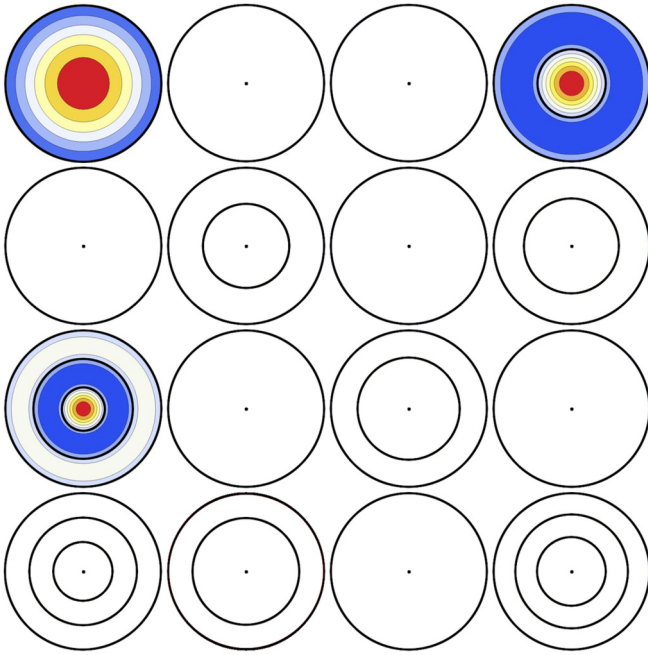


FIG. 17. Representing the cylindrical box wave functions in Fig. 15 to emphasize the differences between the nondegenerate $\Psi_{0,p}(\rho, \phi)$ and the infinitely degenerate $\Psi_{m,p}(\rho, \phi)$ for $m \geq 1$.

Nambu representation. Since the bottom of the box is not a symmetry plane, there are no reflection planes.

VII. THE DISK MICROSTRIP ANTENNA

The thin disk microstrip antenna has been studied previously [19]. Here we include it for two reasons: to compare the wave functions forms with those of the cylindrical box, and to use the degeneracy of the low-energy wave functions to correctly identify the experimentally measured resonant cavity mode emitted from a disk Bi2212 IJJ-THz emitter, which will be described in Sec. VIII.

For the disk MSA, the wave functions also have the form of Eq. (37), but the boundary condition is different:

$$\left. \frac{dJ_m(k_m \rho)}{d\rho} \right|_{\rho=a} = 0. \quad (47)$$

As for the cylindrical box wave functions, there are an infinite number of such wave functions, which have the same forms as in Eqs. (40)–(42), but with the different $\chi_{m,p}$ values appropriate for the disk MSA. The emission frequencies $f_{m,p}$ from

TABLE VI. Representation types, symmetries, and operations of the $C_{\infty v}$ point group for the cylindrical box. The number of circular nodes depends upon p . $R_{\pm m\varphi}$ is a rotation about the centroid by the angle $\pm m\varphi$ and I is the trace of the identity matrix for the appropriate group dimension [10]. See Fig. 17. *Common nodal pattern.

Type	Symmetry	m	Circular nodes	I	$R_{\pm m\varphi}$
A_1	$x^2 + y^2$	0	p	1	1
A_1^*	Centroid node	≥ 1	p	2	$2 \cos(m\varphi)$

TABLE VII. $\chi_{m,p} = k_{m,p}a$ for the disk microstrip antenna of radius a . Missing entries correspond to higher energy states than pictured in Fig. 18.

m	$\chi_{m,1}$	$\chi_{m,2}$	$\chi_{m,3}$	$\chi_{m,4}$
0	3.8317	7.0156	10.1735	13.3237
1	1.8412	5.3314	8.5363	11.7060
2	3.0542	6.7061	9.9695	
3	4.2012	8.0152	11.3459	
4	5.3176	9.2824		
5	6.4156	10.5199		
6	7.5013	11.7349		
7	8.5778			
8	9.6474			
9	10.7114			
10	11.7709			

the 1DR cavity modes (with $m = 0$) and nominally from the 2DR cavity modes (with $m \geq 1$) of the disk MSA are given by [19]

$$f_{m,p} = \frac{c_0 \chi_{m,p}}{2\pi a n_r}, \quad (48)$$

where the lowest group of $\chi_{m,p}$ values are listed in Table VII.

With regard to the 2DR wave functions with $m \geq 1$, the wave functions can be written in Nambu form or for a general $P(\theta) \neq C$ mixing angle distribution, as in Eqs. (44)–(46). Thus the 2DR disk MSA wave functions are all doubly degenerate functions, each component of which can be presented by an infinite number of spatial forms. Figures 18–20 for the disk MSAs are analogous to Figs. 15–17 for the cylindrical boxes. Table VIII presents listings of representation types, symmetries, and C_{3v} symmetry operations for the equilateral triangular MSA wave functions.

In conclusion, for the cylindrical box and disk MSA, there are only two types of wave functions: nondegenerate wave functions with $m = 0$ that have no nodal lines passing through the centroid, and a much larger class of wave functions with $m \geq 1$ that have one or more nodal lines passing through the centroid. When there is no experimental reason, such as by symmetry-breaking hot spots in a cylindrical MSA, to prefer a particular nodal line direction, there are an infinite number of such possible nodal line directions. The rotation matrices $R_{\pm m\varphi}$ for the 2DR MSA wave functions are identical to Eq. (41) for the 2D cylindrical box, with the MSA $k_{m,p}$ values, the lowest-energy values of which are given by Table VII.

TABLE VIII. Representation types, symmetries, and operations of the $C_{\infty v}$ point group for the disk MSA wave functions $\Psi_{m,p}(\phi, \rho)$. The number of circular nodes depends upon p . The $R_{\pm m\varphi}$ are rotations about the z axis normal to the centroid by $\pm m\varphi$ and I is the trace of the identity matrix for the appropriate group dimension [10]. See Fig. 20. *Common nodal pattern.

Type	Symmetry	m	Circular nodes	I	$R_{\pm m\varphi}$
A_1	$x^2 + y^2$	0	p	1	1
A_1^*	Centroid node	≥ 1	$p - 1$	2	$2 \cos(m\varphi)$

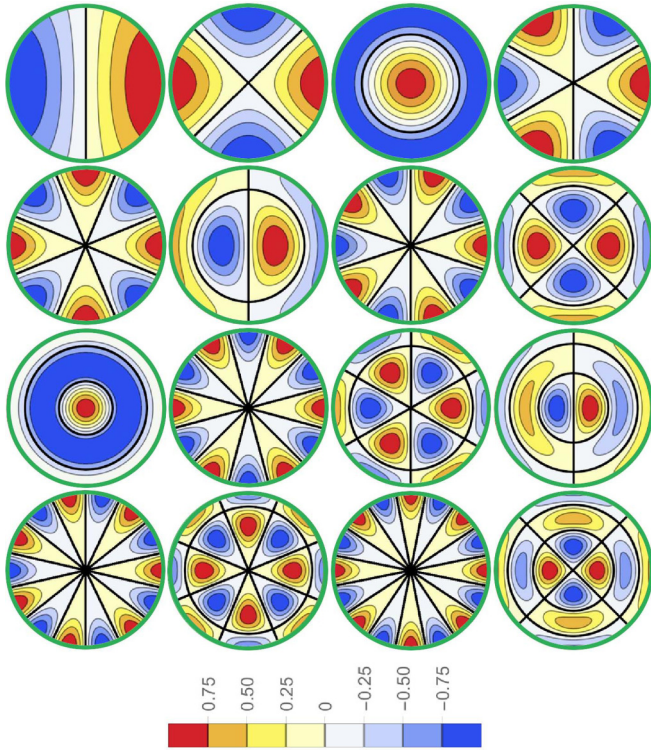


FIG. 18. Lowest frequency wave functions for the disk MSA [19]. $f_{m,p}$ values increase from the top left to the bottom right. Top row, left to right: (1,1), (2,1), (0,1), (3,1). Second row: (4,1), (1,2), (5,1), (2,2). Third row: (0,2), (6,1), (3,2), (1,3). Fourth row: (7,1), (4,2), (8,1), (2,3). The green boundaries indicate the Neumann condition. The color code bars are qualitatively similar but numerically distinct for each of these figures. The color code that varies from -0.92 to $+0.92$ is for the (2,1) mode.

The only difference in symmetry Tables VI and VIII for the cylindrical box and the thin disk MSA is in the number of circular nodes for their 2DR wave functions, which is one more for the box due to the boundary condition. Thus, we conclude that for the thin MSAs, the only modes that can build up a cavity resonance are those of the 1DR wave functions with $m = 0$.

VIII. COMPARISON WITH EXPERIMENTS

Since the original discovery of coherent THz emission from the IJJs in Bi2212 [16], a variety of experimental groups in many countries have been working on the topic, trying to

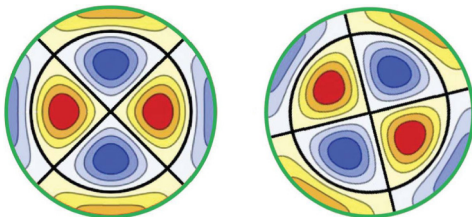


FIG. 19. Comparison of $\Psi_{2,2}(\rho, \phi)$ of the disk MSA with $\theta = 0^\circ$ (left) and $\theta = 31^\circ$ (right).

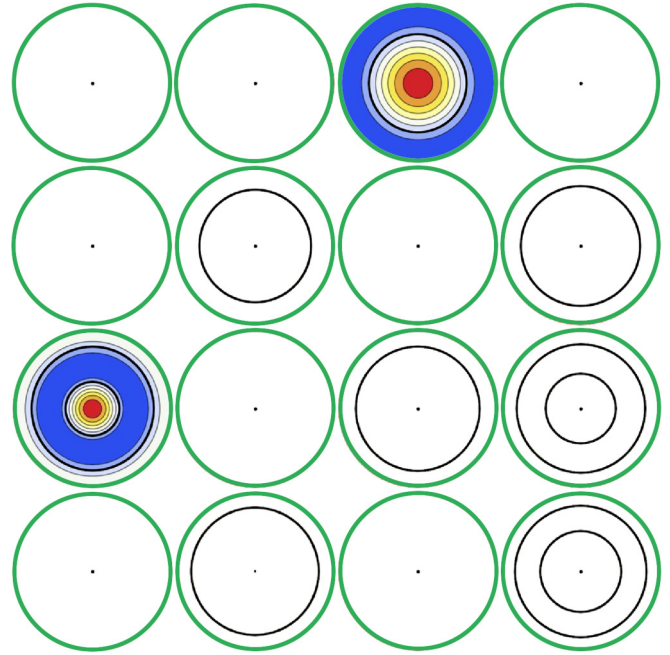


FIG. 20. Plots of the same disk MSA wave functions as in Fig. 18, but with the straight nodal lines passing through the centroid represented by a dot at the centroid for all of the 2DR wave functions.

understand its properties and to increase the output power. There have so far been six review articles on the subject [59–64]. In the early work, the first type of Bi2212 mesas were formed by subjecting a cleaved single crystal of Bi2212 to an Ar beam with a mask, that cut into the unmasked region of the crystal, leaving a standing mesa with the remainder of the Bi2212 crystal as the substrate. A second type was a groove mesa, obtained by simply cutting a groove into the top of a cleaved Bi2212 crystal, which was first done for groove rectangular, square, and disk mesas [49], and subsequently for a groove equilateral triangular mesa [42]. In those experiments, the emission frequencies for three groove disk mesas, the rectangular, the square, and three groove equilateral triangular mesas were all consistent with their respectively lowest-frequency TM(1,1) and TM(0,1) modes [42,49]. For the rectangular mesa, the TM(0,1) mode with a nodal line bisecting the mesa length is nondegenerate and, as expected, was the first shape to be shown to build up a cavity resonance [16]. However, as discussed in Secs. II, V, and VII, the wave functions of those lowest-frequency TM(0,1) square and equilateral triangular modes and the lowest-frequency TM(1,1) disk modes are all doubly degenerate 2DR wave functions of their respective point groups, each component of which can be presented by an infinite number of real space forms. Therefore, if the groove mesas were sufficiently accurately constructed for those symmetries to be relevant, they shouldn't build up cavity resonances at those frequencies [18,19]. The fact that the lowest frequency, doubly degenerate 2DR wave function cavity modes, each component of which can be presented by an infinite number of spatial forms, were observed in those experiments is therefore most likely due to the breaking of the square, equilateral triangular, or disk

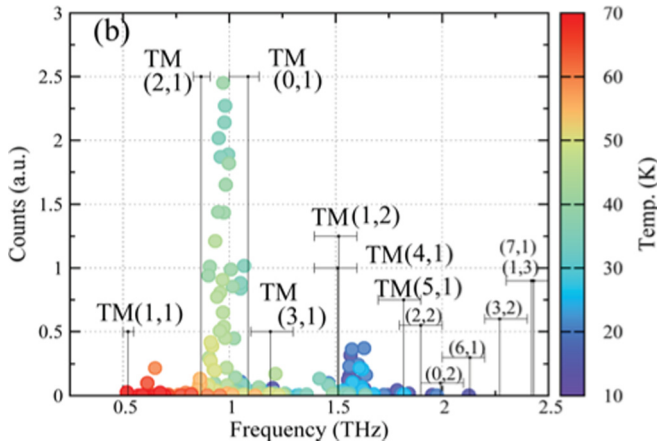


FIG. 21. Frequency dependence of the emission from a stand-alone Bi2212 disk mesa [50]. Reprinted with permission from T. Kashiwagi, K. Sakamoto, H. Kubo, Y. Shibano, T. Enomoto, T. Kitamura, K. Asanuma, T. Yasui, C. Watanabe, K. Nakade, Y. Saiwai, T. Katsuragawa, M. Tsujimoto, R. Yoshizaki, T. Yamamoto, H. Minami, R. A. Klemm, and K. Kadowaki, A high- T_c intrinsic Josephson junction emitter tunable from 0.5 to 2.4 terahertz, *Appl. Phys. Lett.* **107**, 082601 (2015). ©2015 AIP Publishing LLC.

symmetry due to some phenomenon that was not understood at the time of those early experiments.

The problem turned out to be that the introduction of a dc V and current I across the stack of IJJs in Bi2212 leads to severe Joule heating effects, resulting in hot spots, spatial regions in which $T > T_c$ [25–27,32]. For a rectangular Bi2212 mesa, these hot spots were observed by laser scanning [25,26], SiC photoluminescence [27], and thermoreflectance microscopy [32], and when a hot spot develops away from the center of a square, equilateral triangular, or disk mesa, it breaks the symmetry and allows for the emission of photons at the lowest frequency from the respective doubly degenerate 2DR wave function modes, each component of which can be presented by an infinite number of real space forms. But it was suggested that removing the mesa from its superconducting substrate and coating the top and bottom with a perfect electric conductor such as Au, the output power could be enhanced [18,19]. After doubly cleaving a Bi2212 sample from a single crystal, the top and bottom surfaces are first covered with about 50–100 nm of Ag, followed by about 50–100 nm of Au. These mesas with thin Au layers on their top and bottom surfaces are presently known as either as “stand-alone” mesas [30], or as “GBG” for “gold-Bi2212-gold” mesas [37]. Since Au is a superior thermal conductor, as long as the stand-alone mesas are not much thicker than 1–2 μm , it is usually possible to avoid most of the heating problems, including the development of hot spots. An efficient procedure to manufacture the stand-alone Bi2212 mesas was published [30]. In such mesas, the amount of Joule heating was greatly reduced, and it became possible to investigate experimentally the effects of mesa symmetry upon the cavity resonances observed.

In Fig. 21 the frequency dependence of the emission from a Bi2212 stand-alone disk mesa is shown. Unlike the emission data from three groove disk mesas studied earlier [49], the

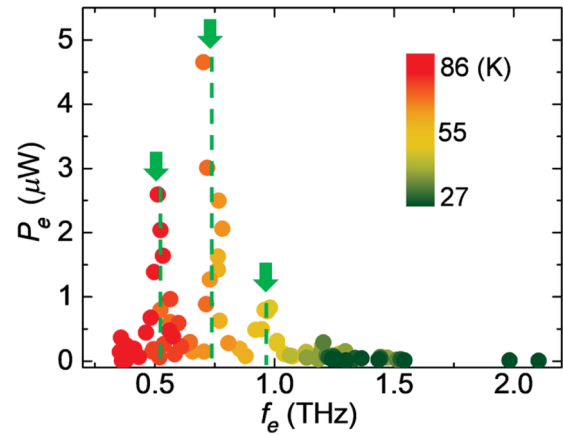


FIG. 22. Frequency dependence of the emission from a square stand-alone Bi2212 mesa [37]. Reprinted with permission from H. Sun, R. Wieland, Z. Xu, Z. Qi, Y. Lv, Y. Huang, H. Zhang, X. Zhou, J. Li, Y. Wang, F. Rudau, J. S. Hampp, D. Koelle, S. Ishida, H. Eisaki, Y. Yoshida, B. Jin, V. P. Koshelets, R. Kleiner, H. Wang, and P. Wu, Compact high- T_c superconducting terahertz emitter operating up to 86 K, *Phys. Rev. Appl.* **10**, 024041 (2018). ©2018 American Physical Society.

stand-alone disk mesa did not build up a cavity resonance at the doubly degenerate, 2DR TM(1,1) disk MSA mode, each component of which can be presented by an infinite number of real space forms. Instead, a strong cavity resonance appeared at 1.0 THz, between the predicted resonance frequencies of the TM(0,1) and TM(2,1) modes. However, since the stand-alone Bi2212 disk mesa was sandwiched in-between two sapphire substrates, the substrates might cause a slight shift in the cavity resonance frequency. Although we are not aware of calculations for a MSA sandwiched between two substrates, when a MSA is sitting atop a sapphire substrate, there is a slight downward shift in the emission frequency [72]. In addition, since the doubly degenerate, 2DR TM(1,1) mode, each component of which can be presented by an infinite number of spatial forms, was not excited, it seems reasonable to assume that the doubly degenerate, 2DR TM(2,1) mode, each component of which can be presented by an infinite number of real space forms, would also not be excited. For those two reasons, we assign the strong emission at 1 THz to the nondegenerate TM(0,1) disk MSA mode. From the data, it appears that the downward frequency shift due to the two sapphire substrates is approximately 3% for emission at 1.0 THz.

We note that the nondegenerate TM(0,2) mode was not excited to form a resonance. Although not pictured in Fig. 21, the authors of that work noted that a small but very narrow resonance-like peak was observed at 2.4 THz. This is about 10%–11% lower than the predicted resonant frequency of the nondegenerate TM(0,3), so if that downward frequency shift were to be due to the sapphire substrate, the substrate shift would have to be rather nonlinear in frequency.

More recently, the emissions from a stand-alone square Bi2212 mesa with $a = 200 \mu\text{m}$ sandwiched between sapphire substrates was studied [37], and the frequency dependence of the emission from that mesa is shown in Fig. 22. From

TABLE IX. Predicted cavity mode frequencies $f_{n,m}$ from Eq. (10), the estimated $f'_{n,m} = 0.97f_{n,m}$ due to the substrate in THz, the degeneracy g of the (n, m) mode for a square stand-alone Bi2212 mesa of side $200 \mu\text{m}$ and $n_r = 4.2$. *At or below the Josephson plasma frequency $f_p \approx 0.250$ THz [21]. †This mode has an accidental degeneracy with the doubly degenerate (1,7) and (7,1) modes, all three of which are 1DR wave functions. See the discussion.

(n, m)	g	$f_{n,m}$ (THz)	$f'_{n,m}$ (THz)
(1,0)	∞	0.179*	0.174*
(1,1)	1	0.253*	0.245*
(2,0)	2	0.357	0.346
(1,2)	∞	0.399	0.387
(2,2)	1	0.505	0.490
(3,0)	∞	0.536	0.520
(3,1)	2	0.564	0.547
(3,2)	∞	0.644	0.625
(4,0)	2	0.714	0.693
(4,1)	∞	0.736	0.714
(3,3)	1	0.758	0.735
(4,2)	2	0.799	0.775
(4,3)	∞	0.892	0.865
(5,0)	∞	0.892	0.865
(5,1)	2	0.910	0.883
(5,2)	∞	0.962	0.933
(4,4)	1	1.010	0.980
(5,3)	2	1.04	1.01
(5,4)	∞	1.146	1.116
(5,5)	3 [†]	1.266	1.228

Eq. (11), it is possible to analyze the emission spectrum in terms of the possible mode frequencies. We note that the authors originally misidentified the cavity resonance mode indices, but corrected them in an erratum [37]. A table of mode indices, the degeneracies, and calculated frequencies without and with a 3% substrate effect is given in Table IX. We note that the lowest two frequencies are at or below the low-temperature Josephson plasma frequency $f_p \approx 0.250$ THz [21], and are screened out by the Josephson plasma.

It is not clear that one should assume the substrate reduction factor to be the same percentage for each frequency measured. But the resonances near to 1.0 THz are likely to have nearly the same shift in the two experiments. Hence, a strong case can be made that the resonances are mostly associated with the nondegenerate (n, n) modes. It is certainly true that the doubly degenerate $(n, n + 2p)$ modes have orthogonal 1DR symmetries, so on some time scale, it would be difficult for the system to stick with one symmetry and to ignore the other one. That is, if the system oscillates between the two symmetries on a time scale inverse to the common mode frequency, there would be no cavity resonance. The data are consistent with this notion [37].

But an interesting question arises about the nonobservation of the 1DR (5,5) mode. Since its emission frequency is predicted to be identical to the doubly degenerate (1,7) and (7,1) modes, this triple degeneracy is “accidental.” In the case of the “accidental” degeneracy between the (0,5), (5,0), (4,3), and (3,4) modes, the unobserved excitation was not predicted to be seen, because each of the four wave functions is a doubly

degenerate 2DR of the C_{4v} point group, each component of which can be presented by an infinite number of real space forms. But the three 1DR MSA wave functions $\Psi_{5,5}(x, y)$, and $\Psi_{1,7}^+(x, y)$, $\Psi_{1,7}^-(x, y)$ respectively have C_{4v} symmetry types A_1 , B_2 , and A_2 , as indicated in Table II. However, we note that the nondegenerate (6,6) mode was also not observed, and this weakening of the resonant modes with increasing frequency was also seen for the disk stand-alone mesa, some of the emission data from which are shown in Fig. 21. So it would be interesting for future experiments to study square stand-alone mesas both smaller and larger in lateral size, in order to respectively examine the resonances from the (1,1) and (6,6) modes, and to verify experimentally the predicted absence of a resonance from the accidentally triply degenerate $\Psi_{5,5}(x, y)$ and $\Psi_{1,7}^\pm(x, y)$ modes.

IX. SUMMARY AND CONCLUSIONS

We studied the wave functions of high-symmetry 2D quantum boxes and electromagnetic microstrip antennas (or cavities). The symmetries studied are those of a square, an equilateral triangle, and a disk. Each of these symmetries has 1D and 2D representations of its wave functions. The two-dimensional representations are doubly degenerate wave functions, each component of which can be presented by an infinite number of spatial forms [10]. The only C_{4v} point group symmetry operation common to these wave functions is their oddness under R_2 , rotations by π about their centroids. In addition, for square boxes and microstrip antennas, there are also doubly degenerate 1D representation wave functions, each component of which can be presented by a single spatial form, the wave functions of which can be written in terms of two orthogonal 1D representations of the C_{4v} point group, differently satisfying all of its symmetry operations.

Although the 2D quantum box might have some approximate experimental relevance to quantum wells, the main interest from the experimental side is for thin microstrip antennas. This is particularly of importance for the coherent THz emission from the intrinsic Josephson junctions in the layered high-temperature superconductor, $\text{Bi}_2\text{Sr}_2\text{CaCu}_2\text{O}_{8+\delta}$, or Bi2212. To date, six review articles have been written on the THz emission from Bi2212 single crystals [59–64]. In the early days of the coherent THz emission from Bi2212, there were severe heating effects that interfered with accurate comparisons of theory with experiment. Now that thermally managed stand-alone Bi2212 (or Au-Bi2212-Au) mesas are the primary devices under study, the effect of the degeneracies of the modes is important to consider. The comparison of the experimental outputs from stand-alone Bi2212 disk and square mesas provide experimental evidence that the nondegenerate modes are the ones that can be excited in order to increase the output power. This suggests that the experimenters should either use stand-alone mesas that have only or predominantly nondegenerate modes, or use a low-symmetry external resonator [38].

The simplest example is that of a rectangle in which the ratio of length to width is not that of two integers, stand-alone mesas of which showed excitations at many frequencies [31]. A singly slitted annulus has been suggested as another possibility [64], and our independent analysis has shown that the

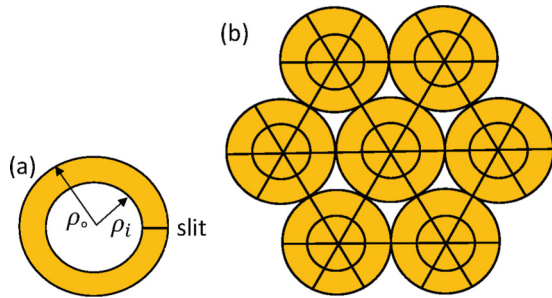


FIG. 23. (a) Sketch of an annular stand-alone mesa with a single slit. (b) Sketch of an array of 84 stand-alone mesas. Seven stand-alone disk mesas are fixed in a hexagonal close packed array, and are equally cut circularly with either a laser or an atomic beam into smaller disks and annuli. Then, with straight line slits, the original disks are each cut into 12 mesas, and the entire array of 84 mesas could be close enough to one another to emit coherently [64].

modes odd and even about the slit are not degenerate [52]. But another possibility is a disk that is cut into 12 pieces of two different types: The disk is first cut into a smaller disk and an annulus by a He or Ar beam or a laser, and those two objects are cut with three straight cuts at angles 60° apart, dividing the smaller disk and annulus into six equivalent pie-shaped wedge mesas and six equivalent hexaslitted annuli. These would all fit closely together, allowing for the possibility of coherent emission from a much larger number of intrinsic Josephson junctions, increasing the output power well above 1 mW. Our studies showed that all of the modes for both mesa shapes are nondegenerate [52].

Such a device has been proposed recently [64], and is redrawn in Fig. 23. In order to maximize the probability of matching the resonant frequencies of the inner pie-shaped wedge mesas with the outer hexaslitted annular mesas, the ratio of ρ_i/ρ_o is varied, and the resonant frequencies can be calculated to find if at least two frequencies from both shapes will match in the 1–2 THz range for which the output power of compact continuous wave coherent sources that to date has been generally less than the 1 mW necessary for practical applications [64].

Since the only equilateral triangular microstrip antennas of Bi2212 were made prior to the construction of stand-alone mesas [42,43], they most likely exhibited hot spots, breaking the symmetry and allowing the ideal doubly degenerate, 2DR TM(0,1) mode, each component of which can be presented in an infinite number of ways, to be observed. We therefore encourage experiments on stand-alone equilateral triangular Bi2212 mesas to compare with our predictions that the lowest observable frequency from a perfect stand-alone equilateral triangular microstrip antenna should be the nondegenerate 1DR TM(0,3) mode, as was done with stand-alone disk and square mesas [37,50].

In addition, we noted in the beginning of the introduction that there has been some confusion regarding the degeneracies in the elementary quantum mechanical 2D box (or infinite square well potential) and in the 2D and 3D simple harmonic oscillator [2–5]. The solutions manuals to the first three texts state that the degeneracy of the first excited state of the 2D box and of the 2D SHO is 2 [2–4], and in Gottfried, the degeneracy

of the first excited state of the 3D SHO was listed as 6 [5]. Although those degeneracies are technically correct, there is a big difference between doubly degenerate 1DR and doubly degenerate 2DR wave functions. The former have only a finite number of possible spatial forms, but each component of the nominally doubly degenerate 2DR wave functions for those particular quantum systems can be presented in an infinite number of spatial forms. This can be shown to be true by including arbitrary mixing angles, such as in Eqs. (6)–(11).

It is interesting to consider perturbation theory that breaks the symmetry of either an infinitely degenerate state or a doubly degenerate 2DR eigenstate with an infinite number of real space forms. That is given in past and current texts for the low-lying states of the 2D box and 2D SHO [2–4], although as stated above, those authors did not appear to recognize the full implications of the degeneracies of those first excited states. This problem is central to many problems in quantum mechanics and for the breaking of the degeneracy of the infinitely degenerate ground state of a Bose-Einstein condensate [65,66]

As noted in Secs. II and III on the square box and square microstrip antenna, there is a distinct difference between a double degeneracy, the wave functions of which obey all of the operations of the relevant point group, in which case the degeneracy is 2, and each of those doubly degenerate wave functions is a 1D representation of the C_{4v} point group, each component of which can be presented by a single spatial form, as shown in Figs. 3 and 7, and those wave functions that are doubly degenerate, 2D representations of that point group, each component of which can be presented in an infinite number of ways, and should properly be pictured only by either just sets of nodal points or sets of nodal points and square boxes, all of which appear to be invariant under all of the operations of C_{4v} . For the equilateral triangular box, the wave functions that are 2D representations of the relevant point group C_{3v} can be represented by either their common nodal points or their common nodal points and equilateral triangular boxes. No such common square or equilateral triangular boxes occur for the square and equilateral triangular microstrip antennas. For the cylindrical box and disk microstrip antenna, there are only nondegenerate, rotationally invariant 1D representations of the point group $C_{\infty v}$, or doubly degenerate, 2D representation wave functions of that point group, each component of which can be presented by an infinite number of real space forms.

For all three box shapes we studied, the ground state is nondegenerate, but the first excited state is a doubly degenerate, 2D representation of its respective point group, each component of which can be presented in an infinite number of ways. For all three thin microstrip antennas we studied, the ground state is a doubly degenerate, 2D representation of the appropriate point group, each component of which can be presented by an infinite number of spatial forms. This has strong experimental consequences, which were shown for the square and disk microstrip antennas. For the square microstrip antenna, the doubly degenerate, 1D representation wave functions, each component of which can be presented only in a single spatial form, did not generate a strong cavity resonance. We emphasize that emission experiments on stand-alone equilateral triangular microstrip antennas have not yet

been made, and should be made, in order to test our predictions that neither the doubly degenerate 1DR wave functions, each component of which can only be presented in a single spatial form, nor the nominally doubly degenerate 2DR wave functions, each component of which can be presented in an infinite number of spatial forms, should generate strong cavity resonances.

Finally, the C_{4v} point group has long been considered to be relevant to the classes of the orbital symmetry of the superconducting order parameter in the cuprates, which includes Bi2212 [22,24,67–71]. Since in the transition metal dichalcogenide $2H$ -TaS₂, the hexagonal symmetry with two or more unit cells normal to the layers gives rise to a nodal charge density wave with an onset at $T_{CDW} = 77$ K [73,74], well above the superconducting $T_c \approx 0.6$ K [12], it seems that such nodal charge density waves could complicate the analysis of many of the existing experiments on Bi2212, particularly if the so-called nodal “pseudogap” that occurs in nanodomains of a monolayer of CuO₂ on top of a freshly cleaved underdoped Bi2212 crystal that survives well above T_c [24], is in fact primarily a charge density wave state, for which the C_{4v} point group would also apply in the absence of orthorhombic splitting of the CuO₂ planes. However, since the pseudogap does not appear in overdoped Bi2212 [71], such experiments should definitely be performed on overdoped samples that are free of the charge-density wave, as was first done by Li *et al.* [67].

ACKNOWLEDGMENTS

The authors acknowledge discussions with Kazuo Kadwaki and Allan H. MacDonald. R.A.K. was supported in part by the U. S. Air Force Office of Scientific Research (AFOSR) LRIR No. 18RQCOR100, and the AFRL/SFFP Summer Faculty Fellowship Program provided by AFRL/RQ at Wright-Patterson Air Force Base. J.R.R., P.Y.C., and A.B. contributed equally to this work. R.A.K. supervised the work and wrote the paper.

APPENDIX

Here we demonstrate that the 2DR wave functions for all three 2D boxes and thin MSAs considered here are orthogonal for any mixing angle θ . First, for both the cylindrical box and thin disk MSA, the components of the upper and lower elements of the Nambu form are for $m \geq 1$ proportional to $\cos[m(\phi - \theta)]$ and $\sin[m(\phi - \theta)]$, as in Eq. (35). Obviously, the inner product $\langle \Psi_{m,p}^{(\theta,1)}(\phi, \rho) | \Psi_{m,p}^{(\theta,2)}(\phi, \rho) \rangle$ is proportional to

$$\begin{aligned} I &= \int_0^{2\pi} d\phi \sin[m(\phi - \theta)] \cos[m(\phi - \theta)] \\ &= \frac{1}{2} \int_0^{2\pi} d\phi \sin[2m(\phi - \theta)] \\ &= \frac{1}{2} \int_0^{2\pi} d\phi \sin(2m\phi) \\ &= 0, \end{aligned} \quad (\text{A1})$$

so these wave functions are orthogonal for any mixing angle θ . For the square box or square microstrip antenna, the 2DR

wave functions are given by Eq. (6) with $\Psi_{n,n+2p+1}(x, y)$ and $\Psi_{n+2p+1,n}(x, y)$, respectively, given by Eqs. (4) and (10) for the square box and MSA. To treat the square box and MSA together, it is useful to define

$$\Psi_{n,m}(x, y) = F_n(x)F_m(y), \quad (\text{A2})$$

where for the box $F_n(x) = \sqrt{2/a} \sin(n\pi x/a)$ for $n, m \geq 1$ while for the square MSA, $F_n(x) = \sqrt{2/a} \cos(n\pi x/a)$ and $n \geq 0$, except that both the x and y functions cannot have $F_0(x)F_0(y)$. Then the inner product in Dirac notation is $I = \langle \Psi_{n,n+2p+1}^{(\theta,+)} | \Psi_{n,n+2p+1}^{(\theta,-)} \rangle$, where

$$\begin{aligned} I &= \int_0^a dx \int_0^a dy \Psi_{n,n+2p+1}^{(\theta,+)*}(x, y) \Psi_{n,n+2p+1}^{(\theta,-)}(x, y) \\ &= \int_0^a dx \int_0^a dy [\cos \theta F_n(x)F_{n+2p+1}(y) \\ &\quad + e^{-i\phi} \sin \theta F_{n+2p+1}(x)F_n(y)] \\ &\quad \times [-\sin \theta F_n(x)F_{n+2p+1}(y) + e^{i\phi} \cos \theta F_{n+2p+1}(x)F_n(y)] \\ &= (\cos^2 \theta e^{i\phi} - \sin^2 \theta e^{-i\phi}) \\ &\quad \times \int_0^a dx F_n(x)F_{n+2p+1}(x) \int_0^a dy F_n(y)F_{n+2p+1}(y) \\ &\quad - \frac{1}{2} \sin(2\theta) \left(\int_0^a dx F_n^2(x) \int_0^a dy F_{n+2p+1}^2(y) \right. \\ &\quad \left. - \int_0^a dy F_n^2(y) \int_0^a dx F_{n+2p+1}^2(x) \right). \end{aligned} \quad (\text{A3})$$

The last line proportional to $\sin(2\theta)$ is easily seen to vanish by interchanging the integration variables x and y . So we have to evaluate the remaining term $(\cos^2 \theta e^{i\phi} - \sin^2 \theta e^{-i\phi})K^2$, where

$$\begin{aligned} K &= \int_0^a dx F_n(x)F_{n+2p+1}(x) \\ &= \int_0^a \frac{dx}{2} (\cos[(2p+1)\pi x/a] \pm \cos[(2n+2p+1)\pi x/a]) \\ &= \frac{1}{2} \frac{a}{\pi(2p+1)} \sin[(2p+1)\pi x/a] \Big|_0^a \\ &\quad \pm \frac{1}{2} \frac{a}{\pi(2n+2p+1)} \sin[(2n+2p+1)\pi x/a] \Big|_0^a \\ &= 0, \end{aligned} \quad (\text{A4})$$

where the \pm refers, respectively, to the MSA (+) and box (−) wave functions. The same conclusion also applies for one of the MSA wave functions independent of position (with $n = 0$), as is easily seen by setting $n = 0$ in the last equation. Hence, all of these 2DR wave functions are indeed orthogonal and infinitely deformable by changing the arbitrary mixing angle θ .

We now generalize this orthornormality to an arbitrary mixing of the two 2DR wave functions $\Psi_{n,n'}^{(\theta,\pm)}(x, y)$, where $n' = n + 2p + 1$, defining

$$\begin{aligned} \Phi_{n,n'}^{(1,2)}(x, y) &= \int_{-\pi}^{\pi} d\theta P(\theta) [A_{1,2} \Psi_{n,n'}^{(\theta,+)}(x, y) \\ &\quad + B_{1,2} \Psi_{n,n'}^{(\theta,-)}(x, y)], \end{aligned} \quad (\text{A5})$$

where the only two restrictions upon $P(\theta)$ are that $P(\theta) \neq C$, for which all of the 2DR wave functions would vanish, and that the integrals in Eq. (11) are finite. Thus, for example, $P(\theta)$ could in principle be an infinite set of Dirac δ functions, as long as the sum of their integrated set was finite.

Using the orthonormality of the 2DR wave functions for either the square box or the MSA, the orthogonality being given in Eq. (A4) and the normality equation being given in elementary textbooks, we can force the above $\Phi_{n,n'}^{(1,2)}(x, y)$ to form a much more general orthonormal set that spans the infinite set of possible θ values. The orthonormality equations are then easily seen for $i = 1, 2$ to be

$$1 = \int_{-\pi}^{\pi} d\theta \int_{-\pi}^{\pi} d\theta' P(\theta)P(\theta') [(|A_i|^2 + |B_i|^2) \cos(\theta - \theta') + (A_i B_i^* - B_i A_i^*) \sin(\theta - \theta')] \quad (\text{A6})$$

$$= (J_e^2 + J_o^2) (|A_i|^2 + |B_i|^2) \quad (\text{A7})$$

and

$$0 = \int_{-\pi}^{\pi} d\theta \int_{-\pi}^{\pi} d\theta' P(\theta)P(\theta') [(A_1 A_2^* + B_1 B_2^*) \cos(\theta - \theta') + (A_1 B_2^* - B_1 A_2^*) \sin(\theta - \theta')] \quad (\text{A8})$$

$$= (J_e^2 + J_o^2) (A_1 A_2^* + B_1 B_2^*). \quad (\text{A9})$$

By interchanging θ and θ' , it is easily seen that the terms containing $\sin(\theta - \theta')$ vanish. Hence, we have for a completely arbitrary $P(\theta)$, that

$$A_1 A_2^* + B_1 B_2^* = 0, \quad (\text{A10})$$

and for $i = 1, 2$, the two identical normalization conditions,

$$|A_i|^2 + |B_i|^2 = [I_e^2 + I_o^2]^{-1}, \quad (\text{A11})$$

where I_e and I_o are given by Eq. (11).

We now provide more details about the orthonormality of the 2DR equilateral triangular box and MSA wave functions from Eqs. (23) and (24). For simplicity of notation, we set $|\Psi_1\rangle = |\Psi_{n,m}^{(e,o,1)}(x, y)\rangle$ and $|\Psi_2\rangle = |\Psi_{n,m}^{(e,o,2)}(x, y)\rangle$ for both the equilateral triangular box and MSA with $m \neq n + 3p$. Then, forcing the two 2DR wave functions to be orthonormal, we require

$$A^2 + B^2 - AB = 1, \quad (\text{A12})$$

$$C^2 + D^2 - CD = 1, \quad (\text{A13})$$

$$AC + BD - \frac{1}{2}(BC + AD) = 0. \quad (\text{A14})$$

Solving Eqs. (A12) and (A13) for B in terms of A and D in terms of C , we have

$$B = \frac{A}{2} \pm \sqrt{1 - 3A^2/4}, \quad (\text{A15})$$

$$D = \frac{C}{2} \pm \sqrt{1 - 3C^2/4}. \quad (\text{A16})$$

These equations force the 2DR equilateral triangular wave functions to be normalized. To force the orthogonality, we have

$$AC + BD - \frac{1}{2}(BC + AD) = 0. \quad (\text{A17})$$

Then, substituting Eqs. (A15) and (A16) into Eq. (A17), we obtain

$$\frac{3}{4}AC + \sqrt{(1 - 3A^2/4)(1 - 3C^2/4)} = 0. \quad (\text{A18})$$

Subtracting the first term from both sides of Eq. (A18), squaring both sides of that equation, and simplifying, we obtain

$$A^2 + C^2 = \frac{4}{3}. \quad (\text{A19})$$

We then choose

$$A = \frac{2}{\sqrt{3}} \cos \theta, \quad (\text{A20})$$

$$C = -\frac{2}{\sqrt{3}} \sin \theta, \quad (\text{A21})$$

which allows for the solutions of both Eqs. (A18) and (A19). Then, from Eqs. (A15) and (A16), we have

$$B = \frac{1}{\sqrt{3}} \cos \theta \pm \sin \theta, \quad (\text{A22})$$

$$D = -\frac{1}{\sqrt{3}} \sin \theta \pm \cos \theta, \quad (\text{A23})$$

and the orthonormal set of 2DR wave equations for the equilateral triangular box of the MSA both indeed form two sets of orthorhombic wave functions, each of which is infinitely deformable by changing the arbitrary mixing angle θ . In the following, we show explicitly that the wave functions in Eq. (25) form an orthonormal set. For simplicity of notation, we write $|\Psi_1\rangle = |\Psi_{n,m \neq n+3p}^{(e,o,1,\theta,\pm)}(x, y)\rangle$ and $|\Psi_2\rangle = |\Psi_{n,m \neq n+3p}^{(e,o,2,\theta,\pm)}(x, y)\rangle$. From Eqs. (A12), (A13), and (A14), we then have

$$\begin{aligned} \langle \Psi_1 | \Psi_1 \rangle &= A^2 + B^2 - AB \\ &= \frac{4}{3} \cos^2 \theta + \left(\frac{1}{\sqrt{3}} \cos \theta \pm \sin \theta \right)^2 \\ &\quad - \frac{2}{\sqrt{3}} \cos \theta \left(\frac{1}{\sqrt{3}} \cos \theta \pm \sin \theta \right) \\ &= \cos^2 \theta \left(\frac{4}{3} + \frac{1}{3} - \frac{2}{3} \right) + \sin^2 \theta \\ &\quad \times \sin \theta \cos \theta \left(\pm \frac{2}{\sqrt{3}} \mp \frac{2}{\sqrt{3}} \right) \\ &= 1, \end{aligned} \quad (\text{A24})$$

$$\begin{aligned} \langle \Psi_2 | \Psi_2 \rangle &= C^2 + D^2 - CD \\ &= \frac{4}{3} \sin^2 \theta + \left(-\frac{1}{\sqrt{3}} \sin \theta \pm \cos \theta \right)^2 \\ &\quad - \left(-\frac{2}{\sqrt{3}} \sin \theta \right) \left(-\frac{1}{\sqrt{3}} \sin \theta \pm \cos \theta \right) \\ &= \sin^2 \theta \left(\frac{4}{3} + \frac{1}{3} - \frac{2}{3} \right) + \cos^2 \theta \\ &\quad + \sin \theta \cos \theta \left(\pm \frac{2}{\sqrt{3}} \mp \frac{2}{\sqrt{3}} \right) \\ &= 1, \end{aligned} \quad (\text{A25})$$

and

$$\begin{aligned}
 \langle \Psi_1 | \Psi_2 \rangle &= AC + BD - \frac{1}{2}(BC + AD) \\
 &= -\frac{4}{3} \sin \theta \cos \theta \\
 &\quad + \left(\frac{1}{\sqrt{3}} \cos \theta \pm \sin \theta \right) \left(-\frac{1}{\sqrt{3}} \sin \theta \pm \cos \theta \right) \\
 &\quad - \frac{1}{2} \left(\frac{1}{\sqrt{3}} \cos \theta \pm \sin \theta \right) \left(-\frac{2}{\sqrt{3}} \sin \theta \right) \\
 &\quad - \frac{1}{2} \frac{2}{\sqrt{3}} \cos \theta \left(-\frac{1}{\sqrt{3}} \sin \theta \pm \cos \theta \right) \\
 &= \cos^2 \theta \left(\pm \frac{1}{\sqrt{3}} \mp \frac{1}{\sqrt{3}} \right)
 \end{aligned}$$

$$\begin{aligned}
 &+ \sin^2 \theta \left(\pm \frac{1}{\sqrt{3}} \mp \frac{1}{\sqrt{3}} \right) \\
 &+ \sin \theta \cos \theta \left(-\frac{4}{3} - \frac{1}{3} + 1 + \frac{1}{3} + \frac{1}{3} \right) \\
 &= 0.
 \end{aligned} \tag{A26}$$

As shown in the main text, it is then elementary to show that all of the 2DR wave functions for the square box and MSA, the equilateral triangular box and MSA, and for the disk box and MSA, are all doubly degenerate, each component of which is infinitely degenerate. For the equilateral triangular box and MSA, the 2DRs also have the \pm extra degeneracy.

-
- [1] D. J. Griffiths and D. J. Schroeter, *Introduction to Quantum Mechanics*, 3rd ed. (Cambridge University Press, Cambridge, 2018).
- [2] J. J. Sakurai, *Modern Quantum Mechanics* (Benjamin/Cummings Publishing, Menlo Park, CA, 1985).
- [3] J. J. Sakurai and J. Napolitano, *Modern Quantum Mechanics*, 2nd ed. (Cambridge University Press, Cambridge, 2017).
- [4] J. J. Sakurai and J. Napolitano, *Modern Quantum Mechanics*, 3rd ed. (Cambridge University Press, Cambridge, 2021).
- [5] K. Gottfried, *Quantum Mechanics, Vol. I: Fundamentals* (Benjamin, New York, 1966).
- [6] H. F. Weinberger, *A First Course in Partial Differential Equations with Complex Variables and Transform Methods* (Blaisdell Publishing, Waltham, MA, 1965).
- [7] H. Weyl, *The Theory of Groups and Quantum Mechanics* (Dover, New York, 1931).
- [8] E. P. Wigner, *Group Theory and Its Application to the Quantum Mechanics of Atomic Spectra* (Academic Press, New York, 1951).
- [9] M. Hammermesh, *Group Theory and Its Application to Physical Problems* (Dover, New York, 1989), Chaps. 2 and 3, pp. 32–114.
- [10] M. Tinkham, *Group Theory and Quantum Mechanics* (McGraw-Hill, New York, 1964).
- [11] B. D. Josephson, Possible new effects in superconductive tunnelling, *Phys. Lett.* **1**, 251 (1962).
- [12] R. A. Klemm, *Layered Superconductors, Vol. 1* (Oxford University Press, Oxford, 2012).
- [13] R. Kleiner, F. Steinmeyer, G. Kunkel, and P. Müller, Intrinsic Josephson Effects in $\text{Bi}_2\text{Sr}_2\text{CaCu}_2\text{O}_8$ Single Crystals, *Phys. Rev. Lett.* **68**, 2394 (1992).
- [14] R. Kleiner and P. Müller, Intrinsic Josephson effects in high- T_c superconductors, *Phys. Rev. B* **49**, 1327 (1994).
- [15] I. E. Batov, X. Y. Jin, S. V. Shitov, Y. Kovel, P. Müller, and A. V. Ustinov, Detection of 0.5 THz radiation from intrinsic $\text{Bi}_2\text{Sr}_2\text{CaCu}_2\text{O}_{8+\delta}$ Josephson junctions, *Appl. Phys. Lett.* **88**, 262504 (2006).
- [16] L. Ozyuzer, A. E. Koshelev, C. Kurter, N. Gopalsami, Q. Li, M. Tachiki, K. Kadowaki, T. Yamamoto, H. Minami, H. Yamaguchi, T. Tachiki, K. E. Gray, W.-K. Kwok, and U. Welp, Emission of coherent THz radiation from superconductors, *Science* **318**, 1149802 (2007).
- [17] K. Kadowaki, M. Tsujimoto, K. Yamaki, T. Yamamoto, T. Kashiwagi, H. Minami, M. Tachiki, and R. A. Klemm, Evidence for a dual-source mechanism of terahertz radiation from rectangular mesas of single crystalline $\text{Bi}_2\text{Sr}_2\text{CaCu}_2\text{O}_{8+\delta}$ intrinsic Josephson junctions, *J. Phys. Soc. Jpn.* **79**, 023703 (2010).
- [18] R. A. Klemm and K. Kadowaki, Angular dependence of the radiation power of a Josephson STAR-emitter, *J. Supercond. Novel Magn.* **23**, 613 (2010).
- [19] R. A. Klemm and K. Kadowaki, Output from a Josephson stimulated terahertz amplified radiation emitter, *J. Phys.: Condens. Matter* **22**, 375701 (2010).
- [20] M. Tsujimoto, T. Yamamoto, K. Delfanazari, R. Nakayama, T. Kitamura, M. Sawamura, T. Kashiwagi, R. Nakayama, T. Kitamura, M. Sawamura *et al.*, Broadly Tunable Subterahertz Emission from Internal Branches of the Current-Voltage Characteristics of Superconducting $\text{Bi}_2\text{Sr}_2\text{CaCu}_2\text{O}_{8+\delta}$ Single Crystals, *Phys. Rev. Lett.* **108**, 107006 (2012).
- [21] E. J. Singley, M. Abo-Bakr, D. N. Basov, J. Feikes, P. Guptasarma, K. Holldack, H. W. Hübers, P. Kuske, M. C. Martin, W. B. Peatman *et al.*, Measuring the Josephson plasma resonance in $\text{Bi}_2\text{Sr}_2\text{CaCu}_2\text{O}_8$ using intense coherent THz synchrotron radiation, *Phys. Rev. B* **69**, 092512 (2004).
- [22] B. W. Hoogenboom, K. Kadowaki, B. Revaz, and Ø. Fischer, Homogeneous samples of $\text{Bi}_2\text{Sr}_2\text{CaCu}_2\text{O}_{8+\delta}$, *Physica C* **391**, 376 (2003).
- [23] E. Borodianskyi and V. Krasnov, Josephson emission with frequency span 1–11 THz from small $\text{Bi}_2\text{Sr}_2\text{CaCu}_2\text{O}_{8+\delta}$ mesa structures, *Nat. Commun.* **8**, 1742 (2017).
- [24] Y. Zhong, Y. Wang, S. Hau, Y.-F. Lv, W.-L. Wang, D. Zhang, H. Dng, Y.-M. Zhang, L. Wang, K. He *et al.*, Nodeless pairing in superconducting copper-oxide monolayer films on $\text{Bi}_2\text{Sr}_2\text{CaCu}_2\text{O}_{8+\delta}$, *Sci. Bull.* **61**, 1239 (2016).
- [25] H. B. Wang, S. Guénon, B. Gross, J. Yuan, A. Iishi, S. Arisawa, T. Hatano, T. Yamashita, D. Koelle, and R. Kleiner, Hot Spots and Waves in $\text{Bi}_2\text{Sr}_2\text{CaCu}_2\text{O}_{8+\delta}$ Intrinsic Josephson Junctions, *Phys. Rev. Lett.* **102**, 017006 (2009).

- [26] H. B. Wang, S. Guénon, B. Gross, J. Yuan, Z. G. Jiang, Y. Y. Zhang, M. Grünzweig, A. Iishi, P. H. Wu, T. Hatano *et al.*, Coherent Terahertz Emission of Intrinsic Josephson Junction Stacks in the Hot Spot Regime, *Phys. Rev. Lett.* **105**, 057002 (2010).
- [27] H. Minami, C. Watanabe, K. Sato, S. Sekimoto, T. Yamamoto, T. Kashiwagi, R. A. Klemm, and K. Kadowaki, Local SiC photoluminescence evidence of hot spot formation and sub-THz coherent emission from a rectangular $\text{Bi}_2\text{Sr}_2\text{CaCu}_2\text{O}_{8+\delta}$ mesa, *Phys. Rev. B* **89**, 054503 (2014).
- [28] R. A. Klemm, E. LaBerge, D. Morley, T. Kashiwagi, M. Tsujimoto, and K. Kadowaki, Cavity mode waves during terahertz radiation from rectangular $\text{Bi}_2\text{Sr}_2\text{CaCu}_2\text{O}_{8+\delta}$ mesas, *J. Phys.: Condens. Matter* **23**, 025701 (2010).
- [29] T. Kitamura, T. Kashiwagi, T. Yamamoto, M. Tsujimoto, C. Watanabe, K. Ishida, S. Sekimoto, K. Asanuma, T. Yasui, K. Nakade *et al.*, Broadly tunable, high-power terahertz radiation up to 73 K from a stand-alone $\text{Bi}_2\text{Sr}_2\text{CaCu}_2\text{O}_{8+\delta}$ mesa, *Appl. Phys. Lett.* **105**, 202603 (2014).
- [30] T. Kashiwagi, T. Yamamoto, H. Minami, M. Tsujimoto, R. Yoshizaki, K. Delfanazari, T. Kitamura, C. Watanabe, K. Nakade, T. Yasui *et al.*, Efficient Fabrication of Intrinsic-Josephson-Junction Terahertz Oscillator with Greatly Reduced Self-Heating Effect, *Phys. Rev. Appl.* **4**, 054018 (2015).
- [31] T. Kashiwagi, T. Yuasa, Y. Tanabe, T. Imai, G. Kuwano, R. Ota, K. Nakamura, Y. Ono, Y. Kanako, M. Tsujimoto *et al.*, Improved excitation mode selectivity of high- T_c superconducting terahertz emitters, *J. Appl. Phys.* **124**, 033901 (2018).
- [32] T. Kashiwagi, T. Tanaka, C. Watanabe, H. Kubo, Y. Komori, T. Yuasa, Y. Tanabe, R. Ota, G. K. K. Nakamura, M. Tsujimoto *et al.*, Thermoreflectance microscopy measurements of the Joule heating characteristics of high- T_c superconducting terahertz emitters, *J. Appl. Phys.* **122**, 233902 (2017).
- [33] T. M. Benseman, K. E. Gray, A. E. Koshelev, W.-K. Kwok, U. Welp, H. Minami, K. Kadowaki, and T. Yamamoto, Powerful terahertz emission from $\text{Bi}_2\text{Sr}_2\text{CaCu}_2\text{O}_{8+\delta}$ mesa arrays, *Appl. Phys. Lett.* **103**, 022602 (2013).
- [34] B. Gross, F. Rudau, N. Kinev, M. Tsujimoto, J. Yuan, Y. Huang, M. Ji, X. J. Zhou, D. Y. An, A. Ishii *et al.*, Electrothermal behavior and terahertz emission properties of a planar array of two $\text{Bi}_2\text{Sr}_2\text{CaCu}_2\text{O}_{8+\delta}$ intrinsic Josephson junctions stacks, *Supercond. Sci. Technol.* **28**, 055004 (2015).
- [35] R. A. Klemm, A. E. Davis, and Q. X. Wang, Terahertz emission from thermally managed square intrinsic Josephson junction microstrip antennas, *IEEE J. Sel. Top. Quantum Electron.* **23**, 41489108 (2017).
- [36] R. A. Klemm, A. E. Davis, Q. X. Wang, T. Yamamoto, D. P. Cerconey, C. Reid, M. L. Koopman, H. Minami, T. Kashiwagi, J. R. Rain *et al.*, Terahertz emission from the intrinsic Josephson junctions of high-symmetry thermally-managed $\text{Bi}_2\text{Sr}_2\text{CaCu}_2\text{O}_{8+\delta}$ microstrip antennas, *Proc. IOP Conf. Mater. Sci. Eng.* **279**, 012017 (2017).
- [37] H. Sun, R. Wieland, Z. Xu, Z. Qi, Y. Lv, Y. Huang, H. Zhang, X. Zhou, J. Li, Y. Wang *et al.*, Compact high- T_c Superconducting Terahertz Emitter Operating up to 86 K, *Phys. Rev. Appl.* **10**, 024041 (2018).
- [38] Y. Ono, H. Minami, G. Kuwano, T. Kashiwagi, M. Tsujimoto, K. Kadowaki, and R. A. Klemm, Superconducting Emitter Powered at 1.5 Terahertz by an External Resonator, *Phys. Rev. Appl.* **13**, 064026 (2020).
- [39] J. Helszajn and D. S. James, Planar triangular resonators with magnetic walls, *IEEE Trans. Microw. Theory Tech.* **26**, 95 (1978).
- [40] P. L. Overfelt and D. J. White, TE and TM modes of some triangular cross-section waveguides using superposition of plane waves, *IEEE Trans. Microw. Theory Tech.* **34**, 161 (1986).
- [41] K. Delfanazari, M. Tsujimoto, T. Kashiwagi, T. Yamamoto, R. Nakayama, S. Hagino, T. Kitamura, M. Sawamura, T. Hattori, H. Minami, and K. Kadowaki, THz emission from a triangular mesa structure of Bi-2212 intrinsic Josephson junctions, *J. Phys.: Conf. Ser.* **400**, 022014 (2012).
- [42] K. Delfanazari, H. Asai, M. Tsujimoto, T. Kashiwagi, T. Kitamura, T. Yamamoto, M. Sawamura, K. Ishida, C. Watanabe, S. Sekimoto *et al.*, Tunable terahertz emission from the intrinsic Josephson junctions in acute isosceles triangular $\text{Bi}_2\text{Sr}_2\text{CaCu}_2\text{O}_{8+\delta}$ mesas, *Opt. Express* **21**, 2171 (2013).
- [43] K. Delfanazari, H. Asai, M. Tsujimoto, T. Kashiwagi, T. Kitamura, T. Yamamoto, M. Sawamura, K. Ishida, M. Tachiki, R. A. Klemm *et al.*, Study of coherent and continuous terahertz wave emission in equilateral triangular mesas of superconducting $\text{Bi}_2\text{Sr}_2\text{CaCu}_2\text{O}_{8+\delta}$ intrinsic Josephson junctions, *Physica C* **491**, 16 (2013).
- [44] R. A. Klemm, K. Delfanazari, M. Tsujimoto, T. Kashiwagi, T. Kitamura, T. Yamamoto, M. Sawamura, K. Ishida, T. Hattori, and K. Kadowaki, Modeling the electromagnetic cavity mode contributions to the THz emission from triangular $\text{Bi}_2\text{Sr}_2\text{CaCu}_2\text{O}_{8+\delta}$ mesas, *Physica C* **491**, 30 (2013).
- [45] D. P. Cerconey, C. Reid, C. M. Doty, A. Gramajo, T. D. Campbell, M. A. Morales, K. Delfanazari, M. Tsujimoto, T. Kashiwagi, T. Yamamoto *et al.*, Cavity mode enhancement of terahertz emission from equilateral triangular microstrip antennas of the high- T_c superconductor $\text{Bi}_2\text{Sr}_2\text{CaCu}_2\text{O}_{8+\delta}$, *J. Phys.: Condens. Matter* **29**, 015601 (2017).
- [46] K. Delfanazari, H. Asai, M. Tsujimoto, T. Kashiwagi, T. Kitamura, M. Sawamura, K. Ishida, T. Yamamoto, T. Hattori, R. A. Klemm, and K. Kadowaki, Experimental and theoretical studies of mesas of several geometries for terahertz wave radiation from the intrinsic Josephson junctions in superconducting $\text{Bi}_2\text{Sr}_2\text{CaCu}_2\text{O}_{8+\delta}$, in *Proceeding 37th International Conference Infrared Millimeter Terahertz Waves, Wollongong, NSW, Australia, 23-28 September* (IEEE, 2012), pp. 1–2.
- [47] K. Delfanazari, H. Asai, M. Tsujimoto, T. Kashiwagi, T. Kitamura, K. Ishida, C. Watanabe, S. Sekimoto, T. Yamamoto, H. Minami *et al.*, Terahertz oscillating devices based upon the intrinsic Josephson junctions in a high temperature superconductor, *J. Infrared Millim. Terahz. Waves* **35**, 131 (2014).
- [48] K. Delfanazari, H. Asai, M. Tsujimoto, T. Kashiwagi, T. Kitamura, T. Yamamoto, W. Wilson, R. A. Klemm, T. Hattori, and K. Kadowaki, Effect of bias electrode position on terahertz radiation from pentagonal mesas of superconducting $\text{Bi}_2\text{Sr}_2\text{CaCu}_2\text{O}_{8+\delta}$, *IEEE Trans. THz Sci. Technol.* **5**, 504 (2015).
- [49] M. Tsujimoto, K. Yamaki, K. Deguchi, T. Yamamoto, T. Kashiwagi, H. Minami, M. Tachiki, K. Kadowaki, and R. A. Klemm, Geometrical Resonance Conditions for THz Radiation from the Intrinsic Josephson Junctions in $\text{Bi}_2\text{Sr}_2\text{CaCu}_2\text{O}_{8+\delta}$, *Phys. Rev. Lett.* **105**, 037005 (2010).
- [50] T. Kashiwagi, K. Sakamoto, H. Kubo, Y. Shibano, T. Enomoto, T. Kitamura, K. Asanuma, T. Yasui, C. Watanabe, K. Nakade *et al.*, A high- T_c intrinsic Josephson junction emitter

- tunable from 0.5 to 2.4 terahertz, *Appl. Phys. Lett.* **107**, 082601 (2015).
- [51] S. Bonnough, Terahertz emission from the intrinsic Josephson junctions of high-symmetry thermally-managed $\text{Bi}_2\text{Sr}_2\text{CaCu}_2\text{O}_{8+\delta}$ annular microstrip antennas, M.S. thesis, University of Central Florida, 2018.
- [52] N. Shouk, R. Shouk, S. Bonnough, and R. A. Klemm, Terahertz emission from thin annular and slitted annular $\text{Bi}2212$ microstrip antennas, in *2020 International Conference on UK-China Emerging Technologies (UCET), 20-21 August* (IEEE, Glasgow, UK, 2020), pp. 1–4.
- [53] H. Asai and S. Kawabata, Control of circularly polarized THz waves from intrinsic Josephson junctions by local heating, *Appl. Phys. Lett.* **110**, 132601 (2017).
- [54] A. Elarabi, Y. Yoshioka, M. Tsujimoto, and I. Kakeya, Monolithic Superconducting Emitter of Tunable Circularly Polarized Terahertz Radiation, *Phys. Rev. Appl.* **8**, 064034 (2017).
- [55] A. Elarabi, Y. Yoshioka, M. Tsujimoto, and I. Kakeya, Circularly polarized terahertz radiation monolithically generated by cylindrical mesas of intrinsic Josephson junctions, *Appl. Phys. Lett.* **113**, 052601 (2018).
- [56] A. Irie, D. Oikawa, and G. Oya, Generation and detection of THz radiation using intrinsic Josephson junctions, *Phys. Procedia* **36**, 199 (2012).
- [57] K. Nakade, T. Kashiwagi, Y. Saiwai, H. Minami, T. Yamamoto, R. A. Klemm, and K. Kadowaki, Applications using high- T_c superconducting terahertz emitters, *Sci. Rep. (UK)* **6**, 23178 (2016).
- [58] Y. Saiwai, T. Kashiwagi, K. Nakade, M. Tsujimoto, H. Minami, R. A. Klemm, and K. Kadowaki, Liquid helium-free high- T_c superconducting terahertz emission system and its applications, *Jpn. J. Appl. Phys.* **59**, 105004 (2020).
- [59] T. Kashiwagi, M. Tsujimoto, T. Yamamoto, H. Minami, K. Yamaki, K. Delfanazari, K. Deguchi, N. Orita, T. Koike, R. Nakayama *et al.*, High temperature superconductor terahertz emitters: Fundamental physics and its applications, *Jpn. J. Appl. Phys.* **51**, 010113 (2012).
- [60] U. Welp, K. Kadowaki, and R. Kleiner, Superconducting emitters of THz radiation, *Nat. Photonics* **7**, 702 (2013).
- [61] I. Kakeya and H. Wang, Terahertz-wave emission from $\text{Bi}2212$ intrinsic Josephson junctions: A review on recent progress, *Supercond. Sci. Technol.* **29**, 073001 (2016).
- [62] T. Kashiwagi, H. Kubo, K. Sakamoto, T. Yuasa, Y. Tanabe, C. Watanabe, T. Tanaka, Y. Komori, R. Ota, G. Kuwano *et al.*, The present state of high- T_c superconducting terahertz emitters, *Supercond. Sci. Technol.* **30**, 074008 (2017).
- [63] R. Kleiner and H. Wang, Terahertz emission from $\text{Bi}_2\text{Sr}_2\text{CaCu}_2\text{O}_{8+x}$ intrinsic Josephson junctions, *J. Appl. Phys.* **126**, 171101 (2019).
- [64] K. Delfanazari, R. A. Klemm, H. J. Joyce, D. A. Ritchie, and K. Kadowaki, Integrated, portable, tunable, and coherent terahertz sources and sensitive detectors based on layered superconductors, *Proc. IEEE* **108**, 721 (2020).
- [65] L. E. Picasso, L. Bracci, and E. d’Emilio, Perturbation theory in quantum mechanics, in *Encyclopedia of Complexity and Systems Science*, edited by R. Meyers (Springer, New York 2009), pp. 6723–6747.
- [66] R. A. van Gorder, Perturbation theory for Bose-Einstein condensates on bounded space domains, *Proc. R. Soc. London A* **476**, 20200674 (2020).
- [67] Q. Li, Y. N. Tsay, M. Suenaga, R. A. Klemm, G. D. Gu, and N. Koshizuka, $\text{Bi}_2\text{Sr}_2\text{CaCu}_2\text{O}_{8+\delta}$ Bicrystal c -Axis Twist Josephson Junctions: A New Phase-Sensitive Test of Order Parameter Symmetry, *Phys. Rev. Lett.* **83**, 4160 (1999).
- [68] R. A. Klemm, C. T. Rieck, and K. Scharnberg, Order parameter symmetries in high-temperature superconductors, *Phys. Rev. B* **61**, 5913 (2000).
- [69] R. A. Klemm, The phase-sensitive c -axis twist experiments on $\text{Bi}_2\text{Sr}_2\text{CaCu}_2\text{O}_{8+\delta}$ and their implications, *Philos. Mag.* **85**, 801 (2005).
- [70] Y. Zhu, M. Liao, Q. Zhang, H.-Y. Xie, F. Meng, Y. Liu, Z. Bai, S. Ji, J. Zhang, K. Jiang *et al.*, Presence of s -Wave Pairing in Josephson Junctions of Twisted Ultrathin $\text{Bi}_2\text{Sr}_2\text{CaCu}_2\text{O}_{8+\delta}$ flakes, *Phys. Rev. X* **11**, 031011 (2021).
- [71] S.-D. Chen, M. Hasimoto, Y. He, D. Soon, K.-J. Xu, J.-F. He, T. D. Devereaux, H. Eisaki, D.-H. Lui, J. Zaanen, and Z.-X. Shen, Incoherent strange metal sharply bounded by a critical doping of $\text{Bi}2212$, *Science* **366**, 1099 (2019).
- [72] C. A. Balanis, *Antenna Theory, Analysis and Design*, 3rd ed. (Wiley, Hoboken, NJ, 2005).
- [73] R. A. Klemm, Pristine and intercalated transition metal dichalcogenide superconductors, *Physica C* **514**, 86 (2015).
- [74] W. C. Tonjes, V. A. Greanya, R. Liu, C. G. Olson, and P. Molinié, Charge-density wave mechanism in the $2H$ - NbSe_2 family: Angle-resolved photoemission study, *Phys. Rev. B* **63**, 235101 (2001).